CHALMERS
UNIVERSITY OF TECHNOLOGY

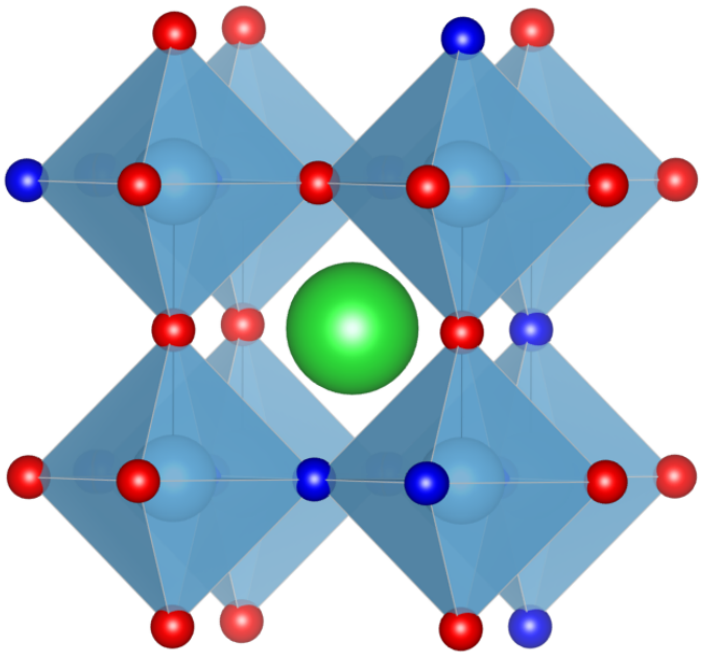

Synthesis and Characterization of Barium Titanate and Barium Indate-Zirconate Perovskite Oxyhydrides

Master's thesis in Nanotechnology

Isac Johansson

DEPARTMENT OF CHEMISTRY AND CHEMICAL ENGINEERING
CHALMERS UNIVERSITY OF TECHNOLOGY
Gothenburg, Sweden 2025
www.chalmers.se

Master's thesis 2025

Synthesis and Characterization of Barium Titanate and Barium Indate-Zirconate Perovskite Oxyhydrides

Isac Johansson

CHALMERS
UNIVERSITY OF TECHNOLOGY

Department of Chemistry and Chemical Engineering
Division of Applied Chemistry
Per-Anders Carlsson's group
Chalmers University of Technology
Gothenburg, Sweden 2025

Synthesis and Characterization of Barium Titanate and Barium Indate-Zirconate Perovskite Oxyhydrides
ISAC JOHANSSON

Examiner: Per-Anders Carlsson, Professor, Division of Applied Chemistry, Department of Chemistry and Chemical Engineering
Supervisor: Rasmus Lavén, Post-Doctoral Researcher, Division of Applied Chemistry, Department of Chemistry and Chemical Engineering

Master's Thesis 2025
Department of Chemistry and Chemical Engineering
Division of Applied Chemistry
Per-Anders Carlsson's group
Chalmers University of Technology
SE-412 96 Gothenburg
Telephone +46 31 772 1000

Cover: General structure of a perovskite oxyhydride of $BaTiO_3$.

Gothenburg, Sweden 2025

Synthesis and Characterization of Barium Titanate and Barium Indate-Zirconate Perovskite Oxyhydrides

ISAC JOHANSSON
Department of Chemistry and Chemical Engeering
Chalmers University of Technology

Abstract

The global imperative to reduce CO_2 emissions has driven interest in catalytic conversion technologies, particularly CO_2 hydrogenation, which transforms CO_2 into valuable chemicals. This reaction often relies on metallic nanoparticles supported on catalyst substrates, commonly metal oxides like Al_2O_3 or ZrO_2. Perovskite oxides have emerged as promising alternatives due to their adjustable surface chemistry, thermal stability, and ability to host redox-active defect sites. Recent attention has turned to anion-adjusted perovskite materials, amongst them oxyhydrides, where oxygen anions are partially replaced by hydride ions. These modifications can enhance catalytic performance and introduce properties such as hydride ion conductivity and interesting electronic and magnetic properties. This project focused on the synthesis and structural analysis of reduced perovskite oxides of synthesised barium titanate ($BaTiO_3$), nano-crystalline barium titanate and barium indate-zirconate ($BaZr_{1-x}In_xO_{3-\frac{x}{2}}$). For $BaTiO_3$, synthesis routes mainly investigated reduction with CaH_2 enclosed in stainless steel capsules, filled with high purity argon. For $BaZr_{1-x}In_xO_{3-\frac{x}{2}}$, reduction by H_2 gas annealing was investigated. Characterization heavily relied on powder X-ray diffraction (PXRD) and thermogravimetric analysis (TGA) measurements. Inelastic neutron scatterin (INS) was performed for a reduced 50% indium substituted $BaZr_{0.5}In_{0.5}O_{2.75}$. The study primarily investigated how synthesis parameters such as molar ratio of CaH_2, temperature, and heating time affect reduction extent, anion composition, phase formation, impurity formation and crystallinity. The CaH_2 reduction of synthesized tetragonal $BaTiO_3$ at 600° C for 48 hours yields reduced products with a cubic phase, accompanied by a colour change from white to dark blue or black. An increased molar ratio of CaH_2 leads to a greater degree of reduction. Rietveld refinements indicate formation of a single phase in these reduced samples. In contrast, samples of nano-$BaTiO_3$ subjected to the same reduction conditions exhibit a lower degree of reduction and show more pronounced two-phase indications. Higher molar CaH_2 ratios result in the formation of Ba_2TiO_4 impurities. These impurity phases can be reduced by decreasing the CaH_2 ratio. For the nano-$BaTiO_3$, a temperature decrease to 580° C doesn't impact Ba_2TiO_4 amounts. Shortening the heating time to 24 hours leads to decreased amounts, at the expense of a lower reduction extent in the nano-$BaTiO_3$ perovskite phase. Hydrogen annealing of $BaZr_{1-x}In_xO_{3-\frac{x}{2}}$ with 50% indium substitution at 800° C for 24 hours and 70% substitution at 650° C for 20 hours give reduced perovskite oxides of barium indate-zirconate. The extent of reduction is comparable between the two compositions. Inelastic neutron scattering (INS) measurements on the 50% $BaZr_{1-x}In_xO_{3-x/2}$ sample indicate minimal hydride incorporation.

Acknowledgements

I would like to express a big thank you to Rasmus Lavén for for his tremendous help throughout these six months, and for giving me the opportunity to do this project. From experimental planning to result analysis and everything in between, Rasmus has been of huge help.
I would also like to thank Guido J.L. de Reijer and Andreas Schaefer for giving assistance with several parts of the experimental synthesis and setup, and Per-Anders Carlsson for his general guidance, insightful discussions and giving me the opportunity to do this project.
Thank you to Jeff Armstrong for performing INS measurements. I would like to thank the division of Applied Chemistry for providing the lab facilities necessary for this project, and for the people at the division for being so helpful and kind for these six months. This work was performed in part at the Chalmers Material Analysis Laboratory, CMAL, thank you. Experiments at the ISIS Neutron and Muon Source were supported by beamtime allocations through a Xpress access proposal 2590151.

Isac Johansson, Gothenburg, June 2025

List of Acronyms

BZO	Barium indate-zirconate oxide
BZOH	Reduced barium indate-zirconate oxide
CIF	Crystallographic Information File
INS	Inelastic Neutron Scattering
n_H	Molar ratio of H^- to $BaTiO_3$
PXRD	Powder X-ray Diffraction
TGA	Thermogravimetric Analysis

Contents

List of Figures

List of Tables

1

Introduction

The global goal of reducing CO_2 emissions is widely recognized and has become a central focus across both environmental policy and scientific research. Part of the solution in reducing carbon emissions sustainably, is by converting CO_2 into e.g biomass feedstock via CO_2 hydrogenation. This process can be facilitated by the presence of catalytic metallic nanoparticles anchored onto catalyst support materials. Commonly, these catalyst supports are metal oxides, such as aluminium oxide (Al_2O_3) or zirconium oxide (ZrO_2) [3, 4]. Perovskite oxides have also been investigated in this context, for e.g. CO_2 conversion to aromatics [5]. Metal oxides have shown to be effective as catalyst supports, due to their tunable surface properties, thermal stability, and ability to interact strongly with active metals [6]. Many oxides, such as CeO_2 and TiO_2, provide oxygen vacancies and defect sites that promote redox reactions and hydrogen spillover [7]. Additionally, their stability under reaction conditions enables long-term operation without deactivation. Studies have shown that adjusting the anionic sites of these (oxide) catalyst supports enhances their interaction with the nanoparticles, which in turn can improve overall catalytic performance [8]. One example of such anion-adjusted material is oxyhydrides, which show potential as catalyst support materials. These are formed by replacing some of the oxygen atoms (O^{2-}) in oxides with hydride ions (H^-). For ABO_3 perovskite materials, which are the main materials of interest for this project, this occurs according to

$$ABO_3 \rightarrow ABO_{3-x}H_y \tag{1.1}$$

This partial substitution has shown to potentially increase catalytic performance as well as give other interesting properties in e.g. hydride-ion conductivity and catalytic performance in other reactions such as ammonia synthesis [9, 10]. The materials also exhibit interesting electric and magnetic properties which can be tuned by the anionic substitution [9], for instance, several oxyhydride materials exhibit ferroelectric behaviour which in turn can be enhanced by anionic substitution [11].

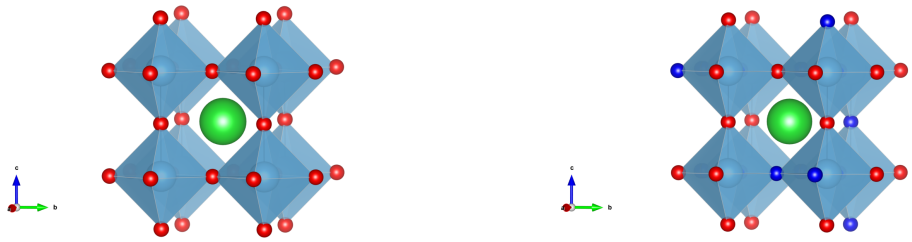

Figure 1.1: a) Typical ABO_3 perovskite structure. **b)** $ABO_{3-x}H_y$ structure where a portion of the oxygen ions have been replaced with hydride ions. Green, light blue and red correspond to A, B and O respectively. Images generated using VESTA software [1].

For perovskite oxyhydrides, A is typically a larger alkaline earth metal cation such as Ba^{2+} or Sr^{2+}, whereas B is a smaller transition metal cation with variable oxidation states e.g. Ti or Co cations. The synthesis requires strongly reducing conditions, but these must be achieved without allowing the hydride, which is itself a powerful reducing agent, to transfer an electron to the metal cation [9]. Overly reducing conditions will hence not yield oxyhydrides, but can rather yield highly reduced metal oxides or the correspondent elemental metal phase. One of the most common ways of reducing the oxides in the synthesis is by metal hydride reduction. For example, CaH_2 can be used as reducing agent. Oxyhydride formation via direct substitution can be written as

$$BaTiO_3 + x\,CaH_2 \rightarrow BaTiO_{3-x}H_x + x\,CaO + \frac{x}{2}\,H_2 \tag{1.2}$$

for $BaTiO_3$ [2]. Recently, it has been shown that it is also possible to form oxyhydrides via direct reduction with H_2(g) [12]. For a indium-substituted barium-zirconate oxyhydride, this process can be described by

$$BaZr_{0.5}In(III)_{0.5}O_{2.75} + 0.25\,H_2 \rightarrow BaZr_{0.5}In(II)_{0.5}O_{2.25}H_{0.5} \tag{1.3}$$

There are also other ways of synthesising oxyhydrides, such as high-pressure solid-state reactions or direct mechanochemical synthesis, starting from binary metal oxides and hydrides [13, 14].

1.1 Aim of the thesis

This project aims to synthesise selected perovskite oxyhydrides of $BaTiO_3$ and $BaZr_{1-x}In_xO_{3-\frac{x}{2}}$ and to conduct structural analysis of the samples using powder X-ray diffraction (PXRD) and thermogravimetric analysis (TGA). Inelastic neutron scattering (INS) is used for selected $BaZr_{1-x}In_xO_{3-\frac{x}{2}}$ oxyhydride samples. The project explores the synthetic strategies for obtaining oxyhydride materials and how these strategies give rise to different properties, such as anion composition, vacancies and overall crystal structure. Molar ratio of CaH_2 to $BaTiO_3$, heating temperature and heating time are the main parameters that are investigated during synthesis. Of the two materials studied in this work, a greater emphasis is put on the oxyhydride

of $BaTiO_3$. This comes naturally as it is more established in previous research and provides a more accessible starting point for method development.

1.2 Outline of the thesis

The structure of the thesis is divided into six chapters. In chapter 2, a theoretical insight into perovskite oxyhydrides will be given, focusing on structural properties and syntheses procedures. Chapter 3 will give a brief and general description of the characterisation methods, as chapter 4 goes into specific detail about the exact experimental procedures. In chapter 5, all results will be presented and discussed, followed by a short conclusion of these results in chapter 6.

2

Perovskite oxyhydrides

This chapter aims to provide an understanding of the theoretical basis of the project, giving insight into oxide & oxyhydride perovskite materials, synthesis procedures and related concepts.

2.1 General structure and properties

Oxyhydrides refer to a class of materials in which some of the oxygen (O^{2-}) from an oxide has been replaced by hydride ions (H^-), making it a mixed anion compound [9]. Examples of early synthesised oxyhydrides are e.g. Ba_3AlO_4H [15] and TiH_xO_y [16]. A very common type of oxyhydrides is transition metal oxyhydrides, where the cations consist of transition metals which normally have varying oxidations states. The varying oxidation states allow for hydride incorporation, since when substituting O^{2-} for H^- (or vacancy), the transition metal atom will be reduced to a lower oxidation state [17]. Hayward et al. were among the first to report a transition metal oxyhydride in 2002, $LaSrCoO_3H_{0.7}$ [18]. The material class of special interest in this report are perovskite transition metal oxyhydrides. "Perovskite" refers to the specific crystal structure of the material, meaning the arrangement of the atoms in the crystal. The classic perovskite oxide nomenclature is ABO_3, making the perovskite oxyhydride $ABO_{3-x}H_y$. A is typically a larger alkaline earth metal cation such as Ba^{2+} or Sr^{2+}, whereas B is a smaller transition metal cation with variable oxidation states e.g. Ti or Co cations. Figure 2.1 displays a typical *cubic* ABO_3 perovskite structure

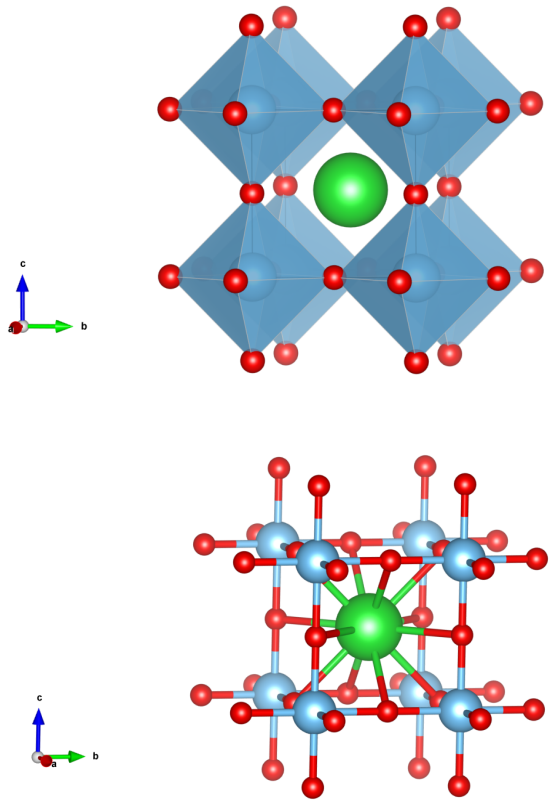

Figure 2.1: Top: Example of ABO_3 perovskite structure. Green, light blue and red correspond to A site, B site and O respectively. **Bottom:** Visualisation of twelve-fold and six-fold oxygen coordination around A and B respectively. Images were generated using VESTA software.

The cubic perovskite unit cell is not uniquely defined, as it can be constructed in different ways, such as by placing either the A-site or B-site cation at the centre of the cell. For visualisation, the unit cell in Figure 2.1 is used as reference. Positioning the A cation at the centre places the B-site cations at the corners of the cubic unit cell. Each B-site cation is coordinated octahedrally by six oxygen atoms. As a result, each A-site cation is coordinated by twelve oxygen atoms from eight neighbouring BO_6 octahedra. When reducing the perovskite, both hydride substitution and vacancy formation is possible.

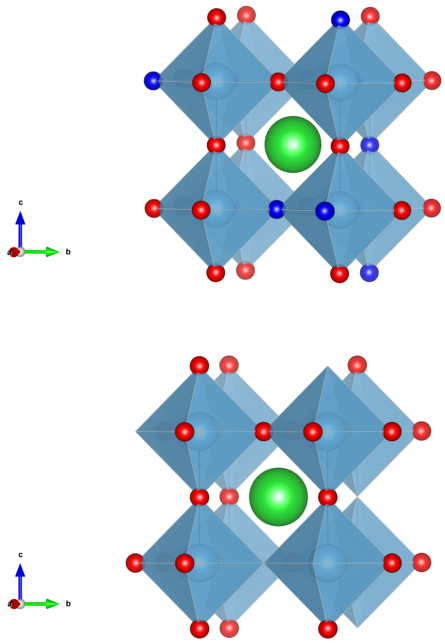

Figure 2.2: Top: $ABO_{3-x}H_y$ structure where a portion of the oxygen atoms have been replaced with hydride ions. **Bottom:** Vacancy formation, where some oxygen has been removed from the perovskite structure. Images were generated using VESTA software.

In Figure 2.2, the oxyhydride and vacancy-filled perovskite phases are shown respectively. Oxygen vacancy formation induces a greater reduction of the transition metal cations, as the removal of O^{2-} gives two excess electrons. In contrast, oxyhydride formation results in a lower degree of reduction, as the introduction of H^- partially compensates the charge imbalance. Although it is theoretically possible to form only one type, upon reduction of a perovskite oxide with H^- available, it is likely that both oxygen vacancies and hydride incorporation occur. For $BaTiO_3$, this has been confirmed [2]. The ABO_3 perovskite oxides already exhibit interesting properties, such as ferroelectricity ($BaTiO_3$) and ferromagnetism ($SrRuO_3$) [19]. Depending on the specific atomic composition, they can be utilized in various areas, including catalytic nitric oxide (NO) conversion reactions and more [20]. Reduction of these perovskite oxides by hydride substitution or vacancy formation alters the electronic band structure of the material [21]. Thus by adjusting the anionic sites and hence the electronic structure, one can enhance existing (electronic, magnetic) properties or introduce new ones. For example, with H^- and O^{2-} having different charges, one can change the oxidation state of the metal atoms, adjust how electrons are arranged around the transition metal centers, and tune inter-cation couplings [21].

2.2 Oxyhydride synthesis

Process	Oxidation	Side products
Vacancy, 1e	$H^- \rightarrow H^\bullet + e$	$0.5(O^{2-} + H_2)$
Vacancy, 2e	$H^- \rightarrow H^+ + 2e$	OH^-
Vacancy, H_2	$H^\bullet \rightarrow H^+ + e$	$0.5H_2O$
Oxyhydride formation	$2H^- \rightarrow H^- + H^\bullet + e$	$0.5(O^{2-} + H_2)$

Table 2.1: Hydrogen processes during hydride reduction, adapted from [2].

There are some different ways of synthesising perovskite oxyhydrides. Generally, synthesis of oxyhydrides is a difficult procedure since one would expect the oxygen and hydrogen to form water under normal conditions. Very reducing conditions are required, making one of the most commonly used methods to reduce the oxide via topochemical metal hydride reduction. Metal hydride reduction is performed by solid state reaction at moderate temperatures. The oxide and metal hydride are mixed together using e.g. ball mill or mortar and pestle. This is normally done in a glove box with inert gas, since metal hydrides are reactive toward H_2O and O_2, causing them to be unstable in air. To avoid any air exposure, the oxide and metal hydride are enclosed in a sealed container, such as a vacuum sealed glass tube or sealed stainless steel capsule. Reaction occur at, for solid state reactions, moderate temperatures (around 400-600° C). The exact reaction mechanisms are not clear and obvious, however the reaction as such is, principally, about removing oxygen in the oxide and replacing them with hydride from the metal hydride. This is a process that has been explored for some time, where the first discovery of a mixed oxyhydride solid of LaHO was made already in 1982 [22]. For perovskite oxides, this synthesis process was first properly investigated and performed by Kobayashi et al. in 2012 [9]. It was discovered that, under strongly reducing conditions with CaH_2 as reducing agent, one can substitute the O^{2-} for H^- in $BaTiO_3$.
Reduction of $BaTiO_3$ using CaH_2 is a reaction that will be heavily investigated in this project. This can take place in a number different of ways [2].
Vacancy formation - one electron process:

$$BaTiO_3 + x\,CaH_2 \rightarrow BaTiO_{3-x} + x\,CaO + x\,H_2 \tag{2.1}$$

Vacancy formation - two electron process:

$$BaTiO_3 + x\,CaH_2 \rightarrow BaTiO_{3-2x} + x\,Ca(OH)_2 \tag{2.2}$$

Vacancy formation, from H_2:

$$BaTiO_3 + x\,H_2 \rightarrow BaTiO_{3-x} + x\,H_2O \tag{2.3}$$

Oxyhydride formation, direct substitution:

$$BaTiO_3 + x\,CaH_2 \rightarrow BaTiO_{3-x}H_x + x\,CaO + \frac{x}{2}\,H_2 \tag{2.4}$$

Oxyhydride formation, via vacancy intermediate:

$$\mathrm{BaTiO_{3-x}} + \frac{x}{2}\,\mathrm{H_2} \rightarrow \mathrm{BaTiO_{3-x}H_x} \tag{2.5}$$

For reduction of $BaTiO_3$ with CaH_2, the notation of n_H will be used. This corresponds to

$$\mathrm{BaTiO_3} + n\mathrm{H}, \quad \text{with } \mathrm{H} = 0.5\,\mathrm{CaH_2} \tag{2.6}$$

It refers to the molar ratio of H^- to $BaTiO_3$. The notation is used to be consistent with previous articles and to facilitate the comparison of reduction with other metal hydrides (e.g. LiH, $NaAlH_4$), as it is mainly the hydride amount that is important rather then amount of metal hydride. An alternative and somewhat less complex method of synthesising (perovskite) oxyhydrides is by reduction with only H_2 gas flow. In 2022, Toriumi et al. managed to reductively hydrogenate a 50 % indium-substituted barium-zirconate perovskite oxide to its reduced oxyhydride derivative via H_2 annealing at 800° C [12]. The reaction is

$$\mathrm{BaZr_{0.5}In(III)_{0.5}O_{2.75}} + 0.25\,\mathrm{H_2} \rightarrow \mathrm{BaZr_{0.5}In(II)_{0.5}O_{2.25}H_{0.5}} \tag{2.7}$$

The authors hypothesise that this process occurs in two consecutive reactions. First, In is reduced from +3 to +1 via

$$\mathrm{BaZr_{0.5}In(III)_{0.5}O_{2.75}} + 0.5\,\mathrm{H_2} \rightarrow \mathrm{BaZr_{0.5}In(I)_{0.5}O_{2.25}} + 0.5\,\mathrm{H_2O} \tag{2.8}$$

followed by oxidative hydrogenation

$$\mathrm{BaZr_{0.5}In(I)_{0.5}O_{2.25}} + 0.5\,\mathrm{H_2} \rightarrow \mathrm{BaZr_{0.5}In(II)_{0.5}O_{2.25}H_{0.5}} \tag{2.9}$$

This reaction gives the final product oxyhydride $BaZr_{0.5}In(II)_{0.5}O_{2.25}H_{0.5}$, in which indium is found to adopt a +2 oxidation state rather than a mixed-valence state of In(I) and In(III) [12]. This is somewhat unexpected, considering that indium has the valence electron configuration ($4d^{10}5s^25p^1$) and would therefore be expected to favour either the +1 or +3 oxidation states, corresponding to the loss of one or three electrons, respectively. The parent oxide of $BaZr_{0.5}In_{0.5}O_{2.75}$ has been rigorously studied because of its proton conductivity in wet atmosphere (H_2O) [23, 24] . One possible way for synthesising a mixed metal cation oxide with In and Zr cations by solid state reaction is

$$\mathrm{BaCO_3} + (1{-}x)\,\mathrm{ZrO_2} + \frac{x}{2}\,\mathrm{In_2O_3} \rightarrow \mathrm{BaZr_{1-x}In_xO_{3-\frac{x}{2}}} + \mathrm{CO_2} \tag{2.10}$$

where x corresponds to the fraction of indium. As can be seen from the general reaction formula, In(III) incorporation inherently brings oxygen vacancy formation. For every two In(III) cations that are integrated in the oxide, one oxygen (O^{2-}) must be removed to compensate for the charge imbalance. Consequently, the indium substituted zirconium oxide has natural oxygen vacancies in the perovskite structure which increase as the fraction of indium increases. Ahmed et al. have synthesised these oxides with $0 \leq x \leq 0.75$ [24], meaning In substitution is possible over a large range. For an ideal 50 % (x=0.5) and 70 % (x=0.7) substitution of In, the reactions are

$$BaCO_3 + 0.5\,ZrO_2 + 0.25\,In_2O_3 \rightarrow BaZr_{0.5}In_{0.5}O_{2.75} + CO_2 \tag{2.11}$$

and

$$BaCO_3 + 0.3\,ZrO_2 + 0.35\,In_2O_3 \rightarrow BaZr_{0.3}In_{0.7}O_{2.65} + CO_2 \tag{2.12}$$

respectively.

2.3 $BaTiO_3$ and $BaTiO_{3-x}H_y$

2.3.1 Structure and properties

As mentioned, Kobayashi et al. managed to synthesise the first perovskite oxyhydride of $BaTiO_3$ in 2012 [9]. These $BaTiO_3$ perovskites can form cubic or tetragonal crystal structure depending on temperature, meaning that in the tetragonal phase one lattice parameter is different from the two other, as opposed to the cubic phase where all three lattice parameters are equal. At room temperature, $BaTiO_3$ is tetragonal. In tetragonal $BaTiO_3$, one lattice parameter is marginally larger then the other two.

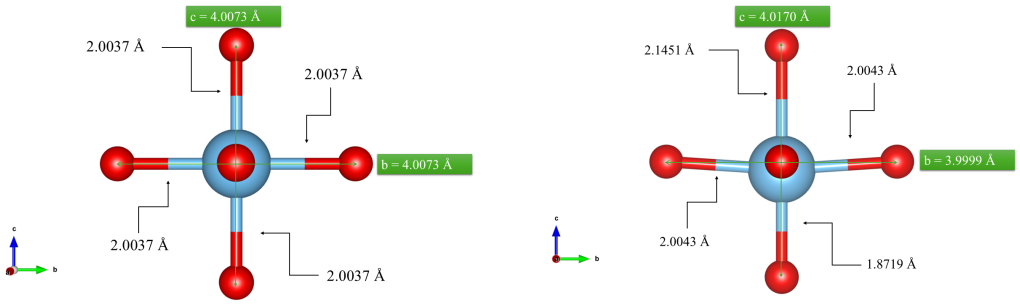

Figure 2.3: Left: Local coordination geometry around Ti in *cubic* $BaTiO_3$. **Right:** Local coordination geometry around Ti in *tetragonal* $BaTiO_3$. Bond lengths are shown for cubic and tetragonal phase respectively [1]. Images were generated using VESTA software.

This effect is illustrated in Figure 2.3. In the tetragonal phase, the Ti ion is displaced along the c-axis, leading to an asymmetry in its position and breaking inversion symmetry [11]. This displacement alters the Ti–O bond lengths and the O–Ti–O bond angles, resulting in an overall distortion of the lattice parameters compared to the undistorted cubic phase of $BaTiO_3$. It is this structural non-centrosymmetric displacement of Ti^{4+} in the tetragonal $BaTiO_3$ structure that gives the material a permanent dipole moment and hence spontaneous electric polarisation, causing it to be ferroelectric [11]. As mentioned, $BaTiO_3$ exhibits different structural perovskite phases depending on temperature. It's rhombohedral at low temperatures, orthorhombic around 183 K, normally tetragonal near 278 K, and eventually transitions to a cubic phase once heated above 396 K [11]. In the oxide, O^{2-} coordinate octahedrally around the Ti(IV) cations. The oxyhydride form of $BaTiO_3$, that is $BaTiO_{3-x}H_y$, has a mix of O^{2-} and H^- ions in the octahedral environment around

the Ti ions. As a result of the change in charge balance, Ti exist in a mixed oxidation state of Ti(III/IV) [9]. Ti(III) has one valence d-electron ($3d^1$) as opposed to Ti(IV) who has an empty 3d shell ($3d^0$). This extra electron increases the ionic radius of the Ti ion leading to an expansion of the perovskite structure, increasing the lattice parameters. This changes the materials long-range average crystal symmetry, and causes the oxyhydride material to be of cubic phase at all temperatures, as opposed to its parent oxide [11][25]. The lattice expands not only as a result of Ti cation radius, but also because the H^- radius is larger then the O^{2-}, and the Ti-anion bond gets weaker [26]. Inclusion of the electron changes the colour of the material from white to blue. There is some controversy whether this colour change is due to the extra electron creating a polaron (localised electrons) or whether it's delocalised in the electronic band. Schrader et al. suggested the formation of polarons [27], while more recently, Granhed et al. found that the extra electron introduces delocalised electronic states in the band gap structure [28].

2.3.2 Previous synthesis reports

Metal hydride reduction of $BaTiO_3$ was first performed by Kobyashi et al. where they reported the formation of oxyhydride $BaTiO_{2.4}H_{0.6}$ [9]. However, synthesis conditions were explored much more extensively by Nedumkandathil et al. in 2018 [2]. The article from 2018 thoroughly explored $BaTiO_3$ reduction with regards to use of different metal hydrides in different molar ratios as well as different heating times for samples with constant molar ratio. Nedumkandathil et al. found several interesting results with regards to reduction with different molar ratio of CaH_2. The following results are collected from [2], used as a basis for comparison

n_H	Product phase/fraction (w%)	Lattice parameters (Å)	x from TG
0 ($BaTiO_3$)	tetragonal	a = 3.9964(1), c = 4.0310(1)	0
0.2	tetragonal	a = 3.9971(1), c = 4.0260(1)	0.03
0.6	cubic	4.0051(6)	0.10
1.2	cubic-I/89(1) cubic-II/11(1)	4.0096(2) 4.0219	0.24
1.8	cubic-I/89(1) cubic-II/11(1)	4.0138(1) 4.0288	0.34

Table 2.2: Synthesis results reported from Nedumkandathil et al. for CaH_2 reduction of $BaTiO_3$ heated at 600° C for 48 hours, table adapted from the original source [2].

Based on x (for $BaTiO_{3-x}H_y$) and the lattice parameters increasing for higher CaH_2 molar ratio, they find that the extent of reduction increases as n_H increases. This trend is consistent for n_H = [0.6 ; 1.2 ; 1.8], however for n_H = 0.2 they still see a tetragonal phase and attain $x = 0.03$ from TGA, indicating little reduction. For 1.2 H and 1.8 H they identify the formation of two separate cubic phases. One majority phase (89 %) with smaller lattice parameter, and one minority phase (11 %) with a larger lattice parameter. This differs from the 0.6 H sample with only one cubic phase, seemingly corresponding to the majority phase of the samples with higher

CaH_2 concentration. They also report a deepening of the colour from blue to dark blue/black, for increasing n_H [2]. This is in agreement with reports from Kobyashi et al. [9]. With regards to heating time, they studied a sample of 1.2 H for 1, 2, 4 and 7 days respectively.

Heating time (days)	Product phase/fraction (w%)	Lattice parameters (Å)	x from TG
1	cubic-I/91(2) cubic-II/9(2)	4.0093(2) 4.0219(1)	0.24
2	cubic-I/87(2) cubic-II/13(2)	4.0079(1) 4.0205(1)	0.24
4	cubic-I/89(2) cubic-II/11(2)	4.0094(1) 4.0221(1)	0.26
7	cubic-I/70(1) cubic-II/28(1) Ti_3O/2(1)	4.0173(1) 4.0275(1)	0.51

Table 2.3: Synthesis results reported from Nedumkandathil et al. for CaH_2 reduction of $BaTiO_3$ heated at 600° C with 1.2 H for different heating times, table adapted from the original source [2].

For all heating times of the 1.2 H samples, a mixture of two phases of cubic $BaTiO_3$ oxyhydride is reported. The 1, 2- and 4 day experiment yield similar results, with approximately similar weight% distribution between the phases, lattice parameters and x values. For the 7-day experiment, the results show a much higher extent of reduction. The reports of a Ti_3O phase suggest onset of decomposition of $BaTiO_3$ [2].

2.4 $BaZr_{1-x}In_xO_{3-\frac{x}{2}}$ and $BaZr_{1-x}In_xO_{3-\frac{x}{2}-y}H_z$:

For the oxide $BaZr_{1-x}In_xO_{3-\frac{x}{2}}$ structure, Ahmed et al. found that all samples, for $0 < x < 0.75$, possessed a cubic symmetry in the perovskite structure [24].

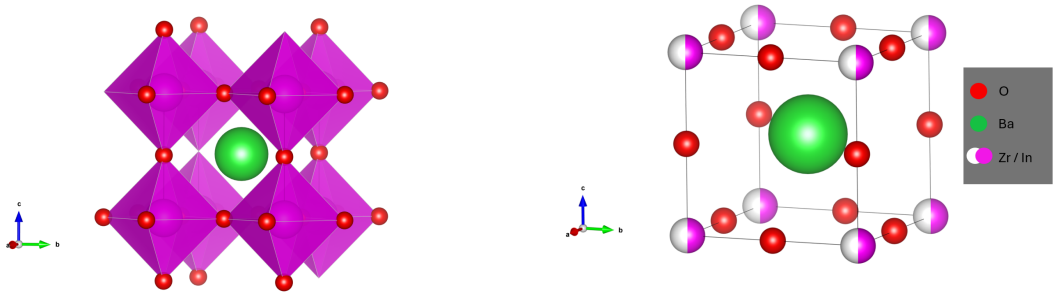

Figure 2.4: Left: Cubic perovskite structure of barium indate zirconate, with some oxygen vacancies as In^{3+} partially replaces the Zr^{4+}. **Right:** Visualisation of partial indium substitution at zirconium atomic positions. Images were generated using VESTA software.

As seen in Figure 2.4, the substitution of Zr^{4+} for In^{3+} cations brings oxygen vacancies. For every two In^{3+} ions that are incorporated, one oxygen vacancy is formed. These already existing oxygen vacancies should facilitate hydride ion incorporation. Ahmed et. al. also found that the size of the lattice parameters increase linearly with increased indium concentration, which comes as a result of the larger ionic radius of In^{3+} compared to Zr^{4+} [24]. Recently, in 2022, Toriumi et al. presented a oxyhydride of a 50% indium substituted zirconium oxide ($BaZr_{0.5}In(II)_{0.5}O_{2.25}H_{0.5}$) [12]. They could demonstrate good H^- ion conductivity and also explored the crystallographic sites at which hydride ions were incorporated into the structure. Using neutron diffraction, they found that hydride could be incorporated into oxygen vacancy sites (3d) but also at interstitial sites close to [100] face centre sites (demonstrated below).

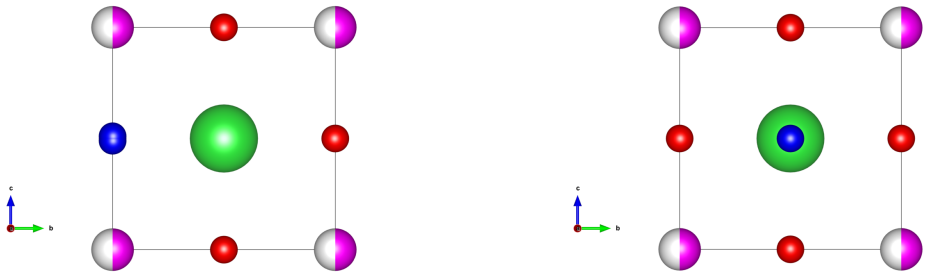

Figure 2.5: Left: Hydride incorporation at oxygen 3d sites. **Right:** Hydride incorporation at interstitial [100] face centre position. Images were generated using VESTA software.

Thanks to their high H^- ion conductivity and relatively simple synthesis procedure, this barium indate-zirconate perovskite oxyhydride show potential for use in ceramic electrolysis cells and membrane reactors for processes like ammonia synthesis, CO_2 hydrogenation, and methane conversion [12].

3

Methods

To characterize the oxyhydrides, powder X-ray diffraction (PXRD) and thermogravimetric analysis (TGA) was used. This chapter aims to provide theoretical insight into these characterization techniques, explaining what they are and how they work. Inelastic neutron scattering (INS) measurements was conducted on selected barium indate-zirconate samples, and is hence briefly described in this section.

3.1 Powder X-ray diffraction

In chemical synthesis there is an evident need of characterising your samples. This characterisation is performed for many reasons, but mainly to find out whether the synthesis has been successfully completed or not. For solid state chemistry synthesis, specifically if your materials are crystalline, powder X-ray diffraction (PXRD) is perhaps the most important and necessary technique. It allows one to determine information regarding the crystal structure such as phases (single, multi) and lattice parameters.

3.1.1 Bragg's law

The theoretical basis of PXRD lays in the fact that electron densities around atoms in a material can diffract electromagnetic waves (EM), such as X-rays, that penetrate through the sample. For an amorphous (no long-range order) material, this diffraction will be disordered/destructive. If the sample material atoms are of an longe range ordered and symmetric nature, that is crystalline, the diffraction of EM waves can occur constructively. Constructive interference can only occur if the distance between two parallel, direction-specific atomic planes is exactly equal to an integer multiple of the wavelength of the X-ray [29]. In order to visualise why this is true see Figure 3.1.

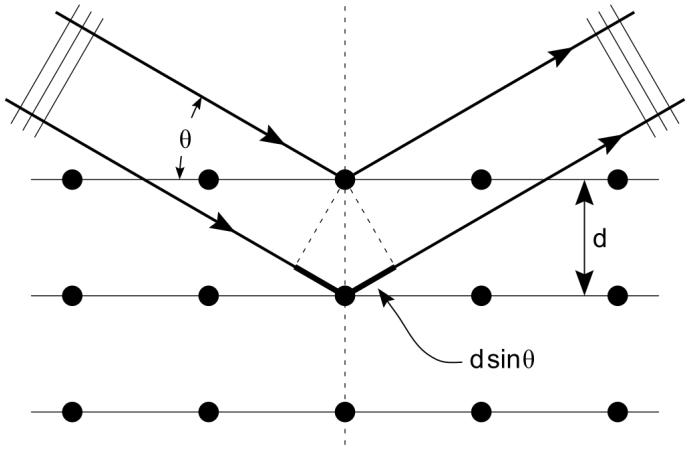

Figure 3.1: Constructive interference of X-rays.

Shall the X-rays interact constructively, they must reach the detector at the same point across the wave, meaning the waves are parallel once they reach the detector. For this to happen, the extra distance that the more penetrative wave travels needs to be an integer multiple of the wavelength. The extra distance can be determined using simple trigonometry relations utilizing the interplanar spacing d and the incident angle of the X-ray θ. This reasoning ultimately leads to Bragg's law

$$2d\,sin(\theta) = n\lambda \tag{3.1}$$

Where $2d\,sin(\theta)$ corresponds to the extra distance travelled [29].

3.1.2 Rietveld refinement and diffraction profile effects

A powerful method to extensively analyse obtained diffraction data is the Rietveld refinement method. It can be used for both neutron diffraction and powder diffraction, where the focus will be on PXRD applications. The method is based on an iterative fitting of calculated diffraction patterns based on structural and instrumental parameters, to experimental diffraction data [30]. By utilizing a reasonably good initial approximation of some parameters, such as unit cell dimensions and atom coordinates, one can refine these parameters (+ other parameters) to calculate a better fit to the experimental data, and hence obtain more accurate crystallographic information for their samples. When used correctly, with good initial guesses and high quality data, it can give reliable information about e.g. lattice parameters, phase quantities, crystal sizes and micro-strain. The goal for a Rietveld refinement is to minimize the difference between the observed diffraction pattern and the calculated pattern generated from a structural model, also known as the difference curve. Rietveld refinement utilizes a non-linear least square method to do this, where a function M is defined as

$$M = \sum_i W_i(I_i^{obs} - I_i^{calc})^2 \tag{3.2}$$

where I_i^{obs} and I_i^{calc} correspond to intensity data for the experimental and calculated profiles respetively, and W_i is a statistical weight factor [31]. The I_i^{calc} is itself defined

as a function of p_n.

$$I_i^{calc} = f(p_1, p_2, ...p_n) \tag{3.3}$$

$I^{calc}(p_n)$ is non-linear and depend on transcendental functions (sin, cos etc.) and can hence not be solved for directly [31]. One has to Taylor expand $I^{calc}(p_n)$ and then solve a set of matrix equations iteratively to minimise the function. The exact mathematical derivations are not of focus here, but can be found in e.g. [32]. Lattice parameters, crystal phases and crystallite size are some examples of parameters that are refined. Differences in size of lattice parameters primarily affects diffraction peak positions while, for example, crystallite size affects the peak shape. Smaller crystallites generally result in broader diffraction peaks due to increased uncertainty in the position of lattice planes. This broadening arises because a fewer number of repeating planes in the individual crystals limits the extent of constructive interference between scattered X-rays [33], as described by the Scherrer equation

$$\tau = \frac{K\lambda}{\beta cos(\theta)} \tag{3.4}$$

where the important thing to note is that if the mean size of the crystalline domains (τ) decrease, the full-width half maximum (β) increase [34]. K is a dimensionless shape factor.

Aside from contributions originating from actual relevant structural characteristics, the need for such a refinement method also comes from sample and instrument parameters that give unwanted contributions to the diffraction and detection of X-rays, and hence affects the appearance of the diffraction data. These parameters can impact background contributions, give shifts in peak positions and affect the line profile (the shape of the peaks). Background contributions, for XRD patterns with well-resolved peaks, are normally estimated by either linear interpolation between selected points between peaks or by using empirical/semi-empirical functions to model the contributions [35]. For more complex patterns, with e.g. significant overlap between peaks, the background estimation becomes less straight forward and may require more advanced modelling approaches. Shifting in peak positions (2θ) mostly originates from sample parameters such as surface roughness or sample displacement. Sample displacement refers to whether the sample position, in relation to the incident X-ray beam and detector, is displaced vertically. Sample displacement correction is described differently depending on the geometry of the instrument. The standard geometry used in most PXRD instruments is the Bragg–Brentano geometry, for such instruments the sample displacement can be described with

$$\Delta 2\theta = \frac{-2s\ cos(\theta)}{R} \tag{3.5}$$

where s is the displacement of the sample and R is the radius of the goniometer circle [35].

Optimally, the diffraction peaks in PXRD would appear as δ functions. However, instrumental and sample parameters cause peak broadening. Effects from instrumental parameters generally give Gaussian line profile contributions, while sample effects inflicts a Lorentzian line profile [31].

$$G(\Delta 2\theta, \Gamma) = \sqrt{\frac{4ln2}{\pi\Gamma^2}} e^{\frac{-4ln2(\Delta 2\theta)^2}{\Gamma^2}} \tag{3.6}$$

$$L(\Delta 2\theta, \gamma) = \frac{2}{\pi\gamma} \cdot \frac{1}{1 + (\frac{2 \cdot \Delta 2\theta}{\gamma})^2} \tag{3.7}$$

where Γ and γ are related to the peaks full-width half-maximum (FWHM) and half-width at half-maximum (HWHM) [31, 35]. These effects are best described using peak shape functions (PSF), where two of the most common ones is Voigt and Pseudo-Voigt. Voigt PSFs are defined as the convolution of $G(\Delta 2\theta, \Gamma)$ and $L(\Delta 2\theta, \gamma)$

$$V(\Delta 2\theta, \Gamma, \gamma) = G(\Delta 2\theta, \Gamma) \circledast L(\Delta 2\theta, \gamma) \tag{3.8}$$

while Pseudo-Voigt PSFs is represented as a linear combination of the Gaussian and Lorentzian contribution.

$$V_p(\Delta 2\theta, \Gamma, \gamma) = \eta L(\Delta 2\theta, \gamma) + (1 - \eta) G(\Delta 2\theta, \Gamma) \tag{3.9}$$

In the pseudo-Voigt function, η is the mixing parameter that determines the relative contribution of the Lorentzian and Gaussian components. It can take values between 0 and 1, where $\eta = 0$ corresponds to a purely Gaussian peak shape and $\eta = 1$ corresponds to a purely Lorentzian peak shape.

3.2 Thermogravimetric analysis

Thermal analysis consist of a wide range of methods in which the properties of a material is studied as a function of temperature. One such analytic technique which will be utilized is Thermogravimetric analysis (TGA). TGA is utilized in order to determine how the mass of a substance varies with temperature. The sample is placed in a furnace and subjected to progressive temperature changes (normally around 20° C/min) while the mass is simultaneously measured [36]. Consequently the raw data received can be used to plot the sample substance mass as a function of temperature, which in turn can be used to study e.g. phase transitions or decompositions of the material. For this project, TGA measurements will be of importance in order to study the degree of reduction for the synthesised oxyhydride samples. By heating the reduced samples in air, reoxidation of the hydride- or vacancy-containing perovskite structure occurs, allowing quantification of the extent of reduction. The mass gain in reaction

$$BaTiO_{3-x} + O_2 \rightarrow BaTiO_3$$

is monitored to determine this.

3.3 Inelastic neutron scattering

By directing a beam of neutrons toward a solid state sample, letting them interact inelastically with the atom nuclei, one can obtain information about the dynamic

properties of the material, such as atomic/molecular vibration modes [37]. This characterisation technique is called inelastic neutron scattering (INS). When neutrons hit sample nuclei, there needs to be an exchange in both momentum ($\bar{Q}$) and energy (E) in order for an neutron scattering event to be inelastic. This means that

$$\Delta E = E_i - E_f \neq 0 \tag{3.10}$$

$$\Delta \bar{Q} = \bar{k_i} - \bar{k_f} \neq 0 \tag{3.11}$$

where E_i and E_f denotes neutron energy before and after the scattering event, and $\bar{k_i}$ and $\bar{k_f}$ correspond to the neutron wave vector before and after the scattering event. This is different from neutron diffraction where the neutrons scatter elastically (ΔE = 0) and only momentum transfer occur. Most importantly for this project, INS is sensitive to hydrogen following that hydrogen has a large incoherent neutron scattering cross-section [38]. Hydrogen nuclei scatter neutrons strongly, allowing for hydrogen to be detected using INS. This is in contrast to PXRD which relies on electron density, making hydrogen very difficult to detect.

4
Experimentals

This chapter will address and describe the experimental procedures, including all steps of the syntheses as well as the characterization measurements.

4.1 Oxide Synthesis

In order to proceed with the synthesis of actual oxyhydrides, the precursor oxides had to be synthesised. This was performed via solid state reaction of crystalline powders, specific for each oxide material type.
For barium titanate, this was done according to

$$BaCO_3 + TiO_2 \rightarrow BaTiO_3 + CO_2 \tag{4.1}$$

For barium zirconate-indate

$$BaCO_3 + (1-x)\,ZrO_2 + \frac{x}{2}\,In_2O_3 \rightarrow BaZr_{1-x}In_xO_{3-\frac{x}{2}} + CO_2 \tag{4.2}$$

Where x is the amount of successfully substituted indium. During the mixing process, a few millilitres of high-purity (>99.5%) ethanol were added. The addition of liquid ethanol significantly improves the mixing of the solid powders, ensuring sufficient contact between the precursor grains and promoting a uniform mixture. This uniformity should result in a higher reaction yield and a more homogeneous oxide upon heating the mixture.
The synthesis includes heating the powders in alumina crucibles using a box furnace. This procedure includes pressing the powder into a pellet and utilizing the remaining powder to cover the top and bottom side of the pellet in the crucibles. Pellet pressing compacts the powder, increasing proximity of grains and subsequently bettering the conditions for forming the desired oxide. It was performed using a pellet press and belonging die set, forming 20 mm diameter pellets. Cover powder is used as extra safety, to reduce any risk of contaminating the pellet. After heating, only the pellet itself is used as sample.

4.1.1 $BaTiO_3$

Amounts of reactants were chosen to form approximately $5g$ of barium titanate product, where 4.2313 g and 1.7125 g of $BaCO_3$ (>99%, Sigma-Aldrich) and TiO_2 (> 99%, Sigma-Aldrich, Anatase -325 mesh) was weighed respectively to attain equal molar proportions of $BaCO_3$ and TiO_2 ($n_{Ba} \approx n_{Ti}$). The precursors were mixed together and grinded using an agate mortar and pestle.

The grinding process was carried out for approximately 15-20 minutes with around 5 ml of ethanol (>99.5%) added in the beginning. An additional 3 ml ethanol was added in the middle of the mixing once the original 5 ml had evaporated. The powder mixture was heated in a furnace at 900° C for 8 hours. The powder mixture was then ground again for the same duration with same amounts of ethanol, where about 70-80 % of the content was pressed into a pellet and the remaining powder was used to cover the bottom and top of the pellet. The crucible was subsequently heated for 48 hours at 1200° C, optimally forming the desired product, $BaTiO_3$. The cover powder was disposed, and the pellet of $BaTiO_3$ was crushed into a fine powder for XRD measurements and oxide reduction with CaH_2.

Before placed in the glovebox, the powder was heated at 500° C to discharge any adsorbed water content.

4.1.2 $\mathbf{BaZr_{1-x}In_xO_{3-\frac{x}{2}}}$

For 50% In substituted barium-zirconate, amounts of reactants were chosen to form approximately 15 g of barium zirconate-indate product. 9.014 g, 2.8147 g and 3.1703 g of $BaCO_3$ (>99%, Sigma-Aldrich), ZrO_2 (99%, Sigma-Aldrich) and In_2O_3 (Alfa Aesar, 99.9%) was weighed respectively to give molar proportions of barium, zirconium and indium according to $n_{Ba} \approx 0.5\ n_{Zr} + 0.5\ n_{In}$. Using agate mortar and pestle, the three precursor powders were grinded and mixed together. Roughly 5 ml of ethanol (>99.5%) was added and the mix was grinded for 10 minutes. Then, a smaller amount of ethanol was added (2-3 ml) and the mix was grinded for an additional 10 minutes. The powder mix was transferred to two Al_2O_3 (alumina) crucibles and heated in a furnace for 8 hours at 1000° C.

After heating, the powder was once again mortled in the same fashion as previously mentioned (10 + 10 minute grinding and addition of ethanol). Around 70% of the powder was then pressed in to a pellet and placed in a alumina crucible. The remainder of the powder was placed at the bottom and top of the pellet (with pellet in-between), in order to avoid contamination/unwanted diffusion issues.

The crucible, containing pellet and cover powder, was then placed in the furnace for a second time, this time for 72 hours at 1200° C. After heating, the pellet and powder was crushed. The intent was to only crush the pellet and re-use the same cover powder for the third heating, however this was not viable as the powder had "morphed" with the pellet. Consequently the entire content of the crucible (pellet + powder) was mortled together with a few ml of ethanol. A pellet was made once again and powder was placed at the bottom and top of the crucible. The crucible was placed in the furnace for the third time, this time for 48 hours at 1325° C. Upon removal from the furnace, the cover powder could be separated from the pellet using sandpaper, allowing only the pellet to be crushed. The pellet was crushed into a fine powder for XRD measurements and oxyhydride synthesis.

The oxide for 70% substituted barium zirconate was synthesised in the same exact fashion, using the same precursors to give molar proportions of barium, zirconium and indium according to $n_{Ba} \approx 0.3\ n_{Zr} + 0.7\ n_{In}$.

4.2 Oxyhydride Synthesis

In total, three ways of synthesising an oxyhydride was tried. The most frequent and most examined was that of the $BaTiO_3$ reduction with metal hydride CaH_2, consequently heating it in an enclosed stainless steel capsule filled with argon. Metal hydride reduction was performed with both synthesised (microcrystalline) and industrially manufactured nanocrystalline $BaTiO_3$, purchased from Sigma-Aldrich. For synthesised $BaTiO_3$, it was also attempted to conduct metal hydride reduction with CaH_2 under simultaneous (reducing) H_2 gas flow.

For $BaZr_{1-x}In_xO_{3-\frac{x}{2}}$ the oxide was heated in H_2 flow, using the hydrogen gas as reducing agent to form the oxyhydride.

4.2.1 $BaTiO_{3-x}H_y$ and nano-$BaTiO_{3-x}H_y$

A series of measurements with the synthesised $BaTiO_3$ and CaH_2 (Sigma-Aldrich, $\geq$ 97.0%) was made with regards to different molar ratios, more specifically $n_H = [0.5; 1.0; 1.5; 2.0]$. An arbitrary mass of barium titanate was decided for each sample, and the correct stoichiometric amount of calcium hydride was calculated based on that.

n_H / Precursor amount	$BaTiO_3$ (g)	CaH_2 (g)
0.5	0.4999	0.02256
1.0	0.4005	0.0362
1.5	0.3006	0.0406
2.0	0.2995	0.0535

Table 4.1: Weighed precursor amounts for different molar ratios of synthesised $BaTiO_3$ and CaH_2.

All synthesis steps using CaH_2 were conducted in a glove box filled with argon (O_2 < 0.1 ppm, H_2O = 0.6 ppm), to avoid exposure to air and water (see Figure 4.1). Stoichiometric amounts (see table 4.1) of both precursors were separately weighed and subsequently crushed and mixed using agate mortar and pestle. The grinding took place for a longer time compared to the oxide synthesis, about 30-40 minutes, without any ethanol.

Figure 4.1: Glovebox with argon (99,999%, Linde), used for the mixing of CaH_2 and $BaTiO_3$.

After grinding, the powder mix was placed directly into a metal capsule using a spatula and enclosed tightly at both ends by Swagelok caps. In the glovebox, wrenches were used to strongly close the caps, hence ensuring that the sample is surrounded by argon with very low amounts of air entering the capsule. The capsule containing the sample was then transferred to a furnace to be heated.

Figure 4.2: Stainless steel capsule (after use) used for $BaTiO_{3-x}H_y$ synthesis, shown both individually and placed inside the furnace.

All samples in the series were heated at 600° C for 48 hours. For the first two samples, $n_H = [1.0 ; 1.5]$, the entire metal capsule was placed inside a box furnace. However this method was abandoned since the swageloks were extremely difficult to open after heating, most likely as a result of the metal expanding at high temperatures. This problem was avoided for samples with $n_H = [0.5 ; 2.0]$ by using a clam shell type tube furnace with open ends, along with longer metal capsules. Thus allowing heating of one side of the capsule (containing the powder), leaving the other end outside the furnace at room temperature. Consequently, the swageloks were much easier to open.

Generally, the different furnace setups are not believed to affect the results significantly. Temperature and time were closely monitored to try to assure as equal conditions as possible. However, a smaller metal capsule does theoretically lead to higher H_2 pressure in the container, which could potentially affect the reducing conditions. For subsequent syntheses, the tube furnace setup was used.
At this stage, an unwanted phase of barium orthotitanate (Ba_2TiO_4), and highly reduced Ti_3O was detected. In an attempt to remove this impurity, an additional synthesis was performed for the synthesised $BaTiO_3$ where the powder was placed in a aluminium oxide tube inside the metal capsule. This was done to investigate whether the contact between the steel and powder caused this impurity, by e.g. Ti diffusing through the metal. Synthesis in alumina tube was performed with n_H = 2.0, m_{BaTiO_3} = 0.3000 g and m_{CaH_2} = 0.0547 g
The same synthesis procedure was conducted for samples of industrially manufactured nano-crystalline (< 100 nm) $BaTiO_3$ (≥ 99%, Sigma-Aldrich). Samples with n_H = [1.0 ; 2.0] were grinded and heated at 600° C for 48 hours. Based on trial filtration of the synthesised $BaTiO_3$ (described later in this section), an increased amount of precursor material was used to attain more sample product in later filtration steps.

n_H / Precursor amount	nano-$BaTiO_3$ (g)	CaH_2 (g)
1.0	1.0007	0.0903
2.0	1.0005	0.1810

Table 4.2: Weighed precursor amounts for different molar ratios of nano-$BaTiO_3$ and CaH_2.

The Ba_2TiO_4 phase was also apparent for these nano-$BaTiO_{3-x}H_y$ samples. In a further attempt to remove the impurity, a sample with n_H = 2.0 was heated at a lower temperature of 580° C to lower reducing conditions. This was carried out with m_{BaTiO_3} = 1.0003 g and m_{CaH_2} = 0.1809 g. Also, the same sample type was heated for only 24 hours instead of 48 to try and remove the impurity.
In order to see if the increased powder amounts for the nano-$BaTiO_3$ samples had an impact on the synthesis results, a sample was prepared using similar amounts of precursor to those of the synthesised $BaTiO_3$ samples. This was mainly with regards to a suspicion of a two-phase formation, indicated by a slight asymmetry in the XRD peak line profiles.
There was an attempt to perform CaH_2 metal reduction of the synthesised $BaTiO_3$ samples in H_2 flow. The powder mix was placed in an Al_2O_3 boat inside the glovebox, enclosing it in a small box filled with argon in order to minimise air exposure during transfer of the sample.
A separate tube furnace was used for this, which allowed for flow of hydrogen gas. While argon was flowing, the sample was quickly transferred from the small argon-filled box and placed in the furnace (with argon flowing simultaneously). Argon flow was continued at 25 ml/min in an attempt to purge all oxygen before increasing temperature and turning on H_2. After five days of purging, argon flow was lowered to 10 ml/min and H_2 flow was started at 8 ml/min. These conditions were held for 2 hours. Argon flow was then stopped, while H_2 was continued at 8 ml/min and

heating started. The sample was heated for 48 hours at 600° C, same as most of the samples heated in metal capsules.

Reduction of $BaTiO_3$ with CaH_2 typically produces substantial amounts of calcium oxide (CaO) in the reaction, hence the samples of oxyhydride $BaTiO_{3-x}H_y$ had to be washed and filtered in order to discharge any remaining CaO. For washing, each nano-$BaTiO_{3-x}H_y$ sample was added to a beaker with 50 ml, 0.1 M solution of ammonium chloride (NH_4Cl, >99.5%, Riedel-de Haën) in methanol (>99.9%). For the synthesised $BaTiO_{3-x}H_y$, 25 ml 0.1 M NH_4Cl solution was used due to the smaller amount of powder in those samples. The solution was stirred for two hours, using magnetic stirrers. The samples were vacuum filtered using a Buchner flask and funnel, along with a vacuum pump. After filtration, the powder was left on the filter paper to dry for a long duration (15-20 hours).

NH_4Cl reacts with CaO according to

$$NH_4Cl + CaO \rightarrow NH_3 + CaCl_2 + H_2O \tag{4.3}$$

Forming $CaCl_2$, which is highly soluble in methanol and can consequently be filtered away after washing with pure methanol [2].

4.2.2 $BaZr_{0.5}In_{0.5}O_{2.75-x}H_y$ and $BaZr_{0.3}In_{0.7}O_{2.65-x}H_y$

Both the 50 % and 70% barium indate-zirconate oxyhydrides were synthesised in a very similar fashion. For both $BaZr_{0.5}In_{0.5}O_{2.75}$ and $BaZr_{0.3}In_{0.7}O_{2.65}$, the sample powder was placed and spread evenly onto a Al_2O_3 crucible "boat". The crucible was then placed in a quartz tube in a tube furnace. In the gas flow synthesis, Ar (99.999%, Linde) and H_2 gas (99.999%, Linde) were used.

For $BaZr_{0.5}In_{0.5}O_{2.75}$, gas flow experiments were conducted according to the following flowchart:

Ar flow was set at 20 ml/min for 24 hours at 600° C. Ar flow was then lowered to 10 ml/min and H_2 flow was initiated at 8 ml/min, while starting a temperature increase to 800° C. After 1 hour, when 800° C set temperature was reached, Ar was stopped completely and H_2 flow was continued at 8 ml/min. Heating was stopped 24 hours later, with H_2 flow still on. Once temperature had reached circa 150° C, H_2 was switched off and Ar was turned on at 15 ml/min. With room temperature being reached, Ar was turned off and sample was removed from the furnace.

For $BaZr_{0.3}In_{0.7}O_{2.65}$, gas flow experiments were conducted according to the following flowchart:

Heating was initiated in Ar at 25 ml/min. 2 hours later, when temperature had reached 650° C, Ar was lowered to 10 ml/min and H_2 was initiated at 5 ml/min. Ar flow was then stopped, as H_2 was increased to 8 ml/min. Heating was stopped 20 hours later. With room temperature being reached, H_2 was stopped and Ar was turned on at 25 ml/min to purge after which the sample was removed from the furnace.

The samples was exposed to argon gas during the heating in order to dehydrate the sample, as OH^- ions incorporates into position of oxygen vacancies [39].

4.2.3 PXRD measurements

PXRD measurements were conducted using a Bruker D8 Discover diffractometer with a Cu Kα radiation source [40]. All powder samples were measured in variable slit on a zero background, monocrystalline silicon holder, in the range of 2θ = [10-90°]. The obtained powder diffractograms were evaluated using EVA software and GSAS-II [41, 42]. EVA was used for general analysis and to give initial insights about the synthesis results. Phase analysis of the PXRD diffractograms was performed in the software, and was used to confirm/strongly indicate whether the synthesis was successful and to identify impurity phases in the samples, comparing the obtained peaks to a crystallography database in the software.

GSAS-II software was used for Rietveld refinement analysis in order to analyse the PXRD diffractograms in greater detail. The refinement was performed using theoretical/calculated structures obtained from CIF files and standard instrumental files for a Cu Kα source instrument. Crystallographic information was calculated for the samples, mainly for phase identification and to determine lattice parameters.

In the refinement, the background was described as a weighted sum of Chebyshev polynomials. An auto-background was computed to set fixed points in the background, then the background (described by the sum of Chebyshev polynomials) was refined to fit the set background points. Generally, 12-14 polynomials with different weight coefficients were used to accurately describe the background. Aside from the background, all refinements were performed with sample displacement, surface roughness, unit cell parameters, crystallite size, micro-strain and atomic mean square displacement (U) as refinement parameters. Pseudo-Voigt PSFs were used to describe the peak shapes.

From the refinement, only the values for lattice parameters are of interest. Parameters such as crystallite size and strain were refined to improve the line profile fit, but the resulting values are not physically meaningful. For them to be meaningful one would need pre-determined instrument parameters from the specific PXRD instrument, which describe the Gaussian and Lorentzian instrumental contributions to the line profile. The refinement performed in this project used a standard Cu Kα instrument file.

4.2.4 TGA measurements

Before TGA measurements, all CaH_2 reduced $BaTiO_3$ samples were vacuum-dried for 7 hours at 50° to discharge any remaining methanol from the washing process. The instrument for TGA measurements was a Mettler TGA/DSC 3+ [43]. 70 μl aluminium oxide crucibles were used, containing around 10-20 mg of sample powder. Experiments were run in air in a temperature range from 30-900° C, with a ramp rate of 10 ° C/min. An empty crucible was measured and subtracted from all obtained TGA sample curves, to compensate for background noise originating from the crucible. Hence all crucibles were assumed to give approximately the same background contribution.

4.2.5 INS measurements

The sample of $BaZr_{0.5}In_{0.5}O_{2.75-x}H_y$ was sent to the ISIS Neutron and Muon Source, located at the Rutherford Appleton Laboratory in Oxfordshire, United Kingdom, for inelastic neutron scattering (INS) measurements using the TOSCA spectrometer. Measurements were carried out on both the sample and an empty reference to determine background noise. Further details regarding the facilities and the instrument can be found from [44, 45].

5

Results and discussion

There are various interesting comparisons and analyses to be made. This chapter will present the results of the syntheses, mainly on the basis of XRD and TGA measurements.

5.1 Synthesis of $BaTiO_3$

In order to confirm the formation of oxide $BaTiO_3$ in the synthesis and also the phase (tetragonal/cubic), one can simply perform a Rietveld refinement and evaluate how well the calculated pattern fits the experimental diffraction data.

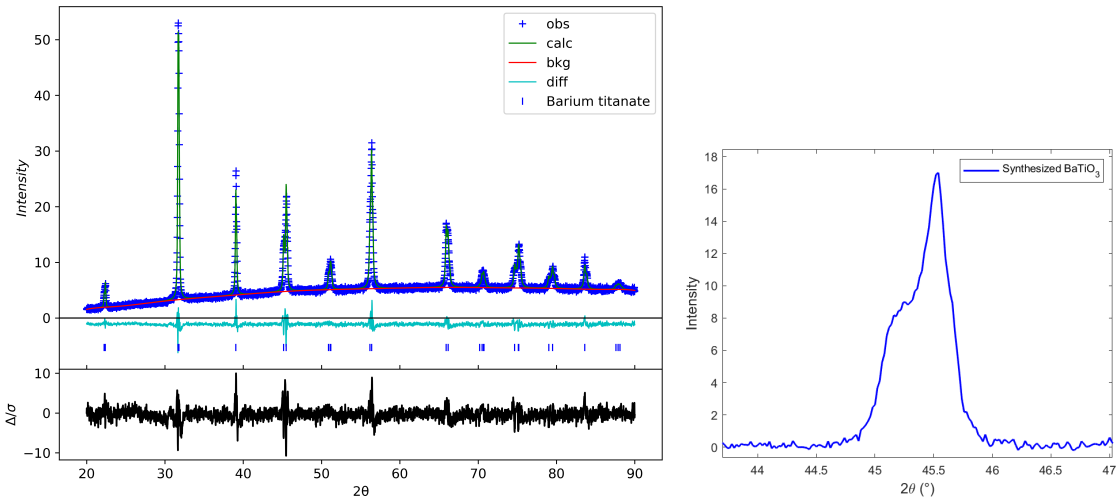

Figure 5.1: Left: Rietveld plot of synthesised $BaTiO_3$. Reference COD ID: 1507756, obtained from Crystallography Open Database. **Right:** Peak split at $2\theta = 45.4^o$, displaying tetragonal phase of $BaTiO_3$. Data was plotted in Matlab.

As depicted in the Rietveld plot to the left in Figure 5.1, the experimental pattern match up well with the reference of tetragonal $BaTiO_3$. This is mainly visualised by the turquoise residual, displaying the difference in intensity values of the experimental and reference pattern. The synthesised $BaTiO_3$ is in tetragonal phase, which is shown in the right panel Figure 5.1. This corresponds to the {200} peak. In tetragonal $BaTiO_3$, as a result of c > b = a, the (002) direction will have a slightly larger lattice parameter, causing the intensity corresponding to that direction to shift to

larger 2θ. This causes the peak split where around 1/3 of the peak intensity shifts. For a cubic phase this peak would be more symmetric.
By further utilizing the Rietveld analysis, the lattice parameters can be compared.

	Lattice parameter (Å)
$BaTiO_3$ synthesised	a = 3.9984(1), c = 4.0257(1)
$BaTiO_3$ reference	a = 3.9999, c = 4.0170

Table 5.1: $BaTiO_3$ lattice parameters for synthesised and reference. Reference COD ID: 1507756, obtained from Crystallography Open Database.

Table 5.1 shows that the c lattice parameter is larger for the synthesised $BaTiO_3$ compared to the reference, while the a lattice parameter is marginally smaller. While it appears that the synthesised oxide is slightly more distorted to tetragonal phase, overall the lattice parameters are very comparable. The reference originates from an article which exploring synthetic methods for $BaTiO_3$, however the exact synthesis conditions corresponding to the reference phase used in this analysis are not specified [46].

5.2 Synthesis of $BaTiO_{3-x}H_y$

The result analysis of the $BaTiO_{3-x}H_y$ oxyhydride will rely heavily on determining the extent to which the $BaTiO_3$ oxide has been reduced. By analyzing the PXRD spectra, including Rietveld refinement analysis, alongside the TGA data, strong indications can be obtained regarding the degree of reduction. As stated in the theory section, the lattice parameter of the perovskite is a strong reflection of the extent of reduction for $BaTiO_3$. A larger lattice parameter indicates a more reduced sample, this will be important for the analysis. All samples presented in this section showed significant colour change from white to dark blue/black, suggesting reduction to some extent.

Figure 5.2: Colours of products from reduction of synthesised $BaTiO_3$ for different concentrations of CaH_2, all heated at 600° C for 48 hours. From left to right, samples are reduced with molar ratios of CaH_2 corresponding to n_H = [2.0 ; 1.5 ; 1.0 ; 0.5].

Figure 5.2 shows a gradient-like colour change, where the colour of the reduced products go from black/dark blue to a lighter blue when CaH_2 concentration decreases. As mentioned in the experimental section, one series of CaH_2 reduction of

synthesised $BaTiO_3$ was made with different molar ratios of CaH_2. PXRD pattern for each $BaTiO_3$ sample heated at 600° C for 48 hours, can be shown in Figure 5.3

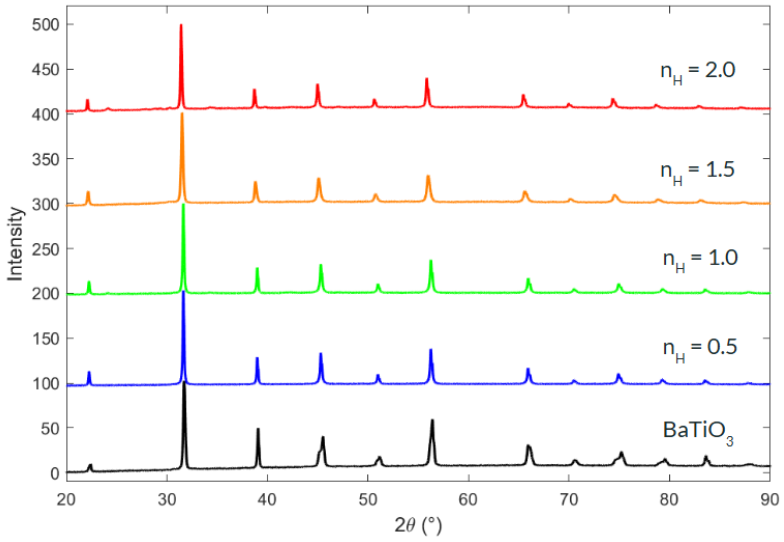

Figure 5.3: PXRD pattern of products from reduction of synthesised $BaTiO_3$ for different concentrations of CaH_2, all heated at 600° C for 48 hours. Peak intensities are normalised to the most intense peak around $2\theta = 31.5^o$. Measured in variable slit. Plotted in Matlab

It is not straightforward to deduce conclusions just looking at Figure 5.3 directly. However, zooming in on one of the peaks reveals some information.

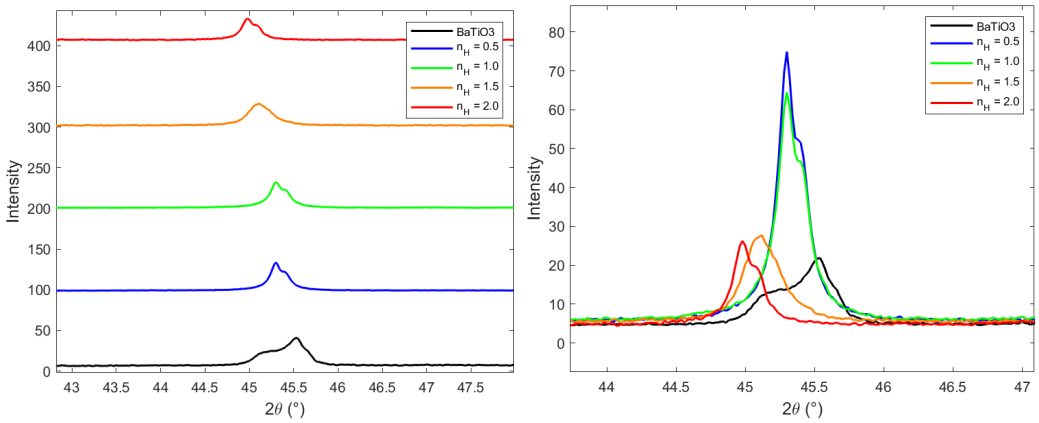

Figure 5.4: Zoomed images of [200] PXRD peak around $2\theta = 45.4^o$. Plotted in Matlab

Looking at Figure 5.4, a general indication can be noted regarding the degree of reduction. Comparing the oxide (black) with the reduced samples (various colors) in the plot, all n_H samples have a shift toward lower 2θ, indicating an increase in lattice parameter consistent with a higher degree of reduction [2]. Samples with higher concentrations of CaH_2 exhibit a more pronounced shift toward lower 2θ angles, indicating a greater extent of reduction. This is not a direct conclusion,

as there are multiple other sample and instrumental parameters that can affect the shift in 2θ. In order to more accurately determine the extent of reduction, one needs to use Rietveld refinement to determine the lattice parameters of the samples. By looking at the line profiles in Figure 5.4, there is a clear difference between the n_H samples and the parent oxide. As previously discussed and visualised in Figure 5.1, the oxide shows a tetragonal line profile. None of the reduced samples exhibits this however, as they show a more sharp and symmetrical line profile, characteristic for a cubic phase. To analyse this further, below are shown the Rietveld plots for all $n_H = [0.5 ; 1.0 ; 1.5 ; 2.0]$ samples, using a cubic $BaTiO_3$ phase as reference.

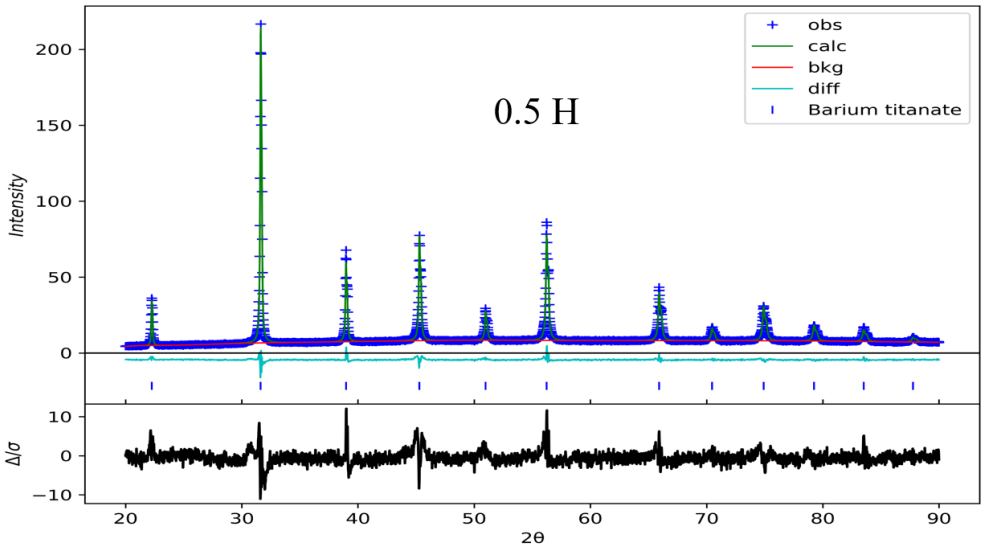

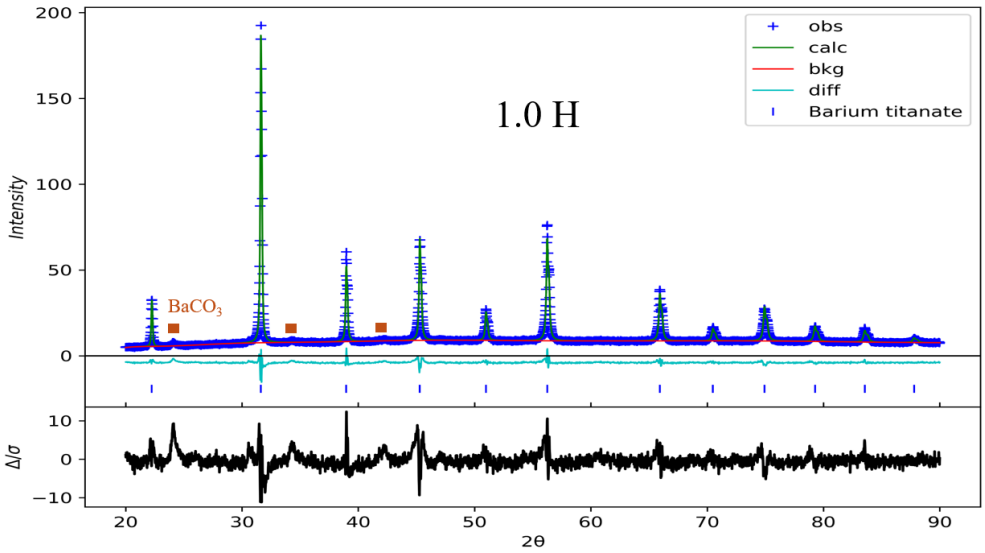

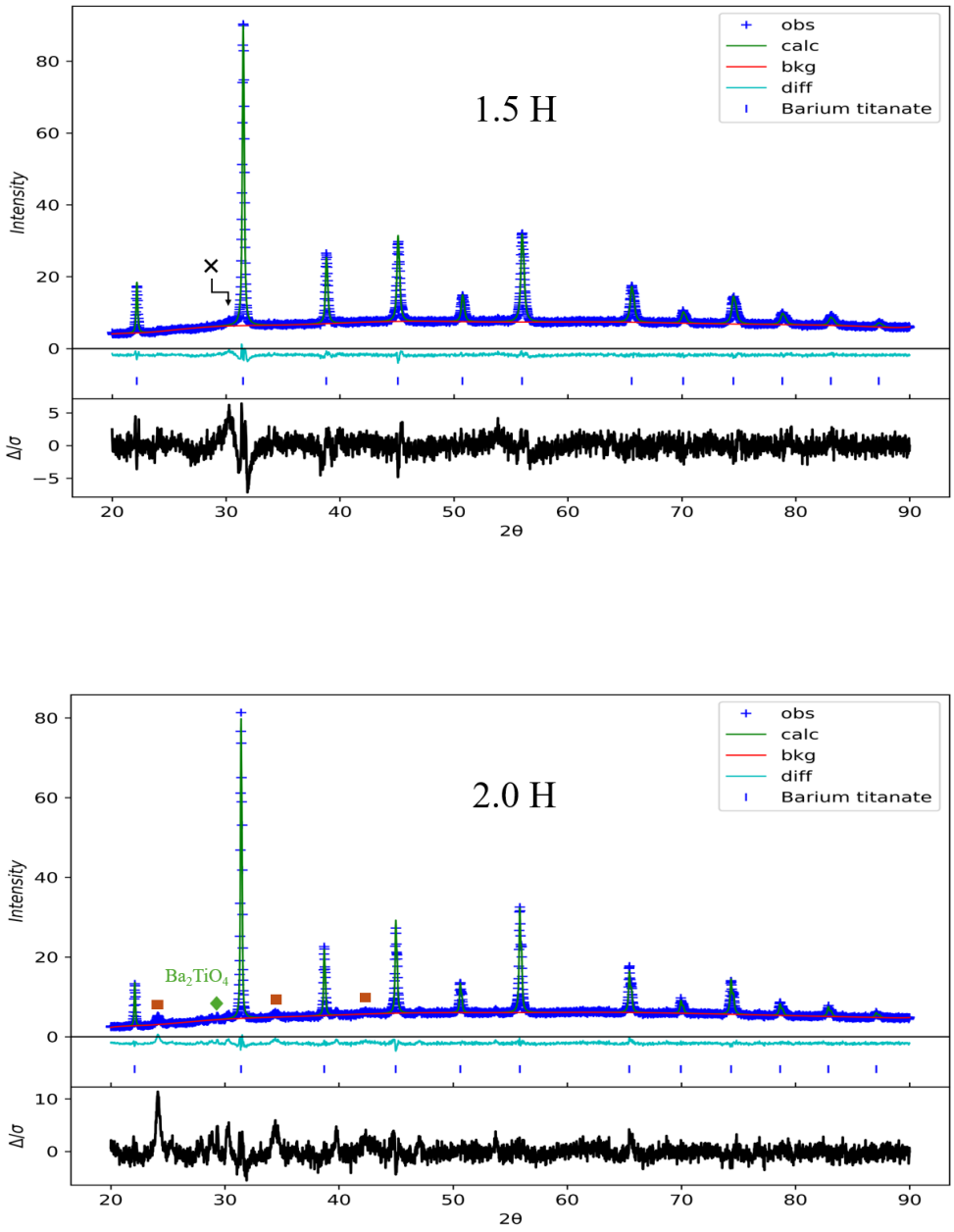

Figure 5.5: Rietveld plots of products from reduction of synthesised $BaTiO_3$ for different concentrations of CaH_2. The blue crosses, green line, and turquoise line correspond to the observed data, calculated fit, and difference curve, respectively. Orange squares mark $BaCO_3$ impurities (1.0 H, 2.0 H), green diamond symbols mark orthorhombic Ba_2TiO_4 impurities (2.0 H). The black cross likely corresponds to a monoclinic Ba_2TiO_4 phase, however this is unconfirmed.

As can be observed directly from the difference curves in the Rietveld plots, they show good agreement between the observed and calculated patterns. There is minimal deviation between the observed data and the calculated curve, indicating a good fit. This can be further analysed by comparing refinement quality indicators, R_{wp} and χ^2.

n_H	R_{wp}	χ^2
0.5	4.451 %	2.56
1.0	4.923 %	3.28
1.5	3.863 %	1.58
2.0	5.144 %	2.14

Table 5.2: Refinement quality indicators for CaH_2 reduced samples of synthesised $BaTiO_3$

Values of R_{wp} vary between 3.863% and 5.144% while χ^2 values vary from 1.58 to 3.28, showing reasonably good fits for all samples. One Rietveld refinement was performed for the 2.0 H sample, using a tetragonal phase $BaTiO_3$ as reference.

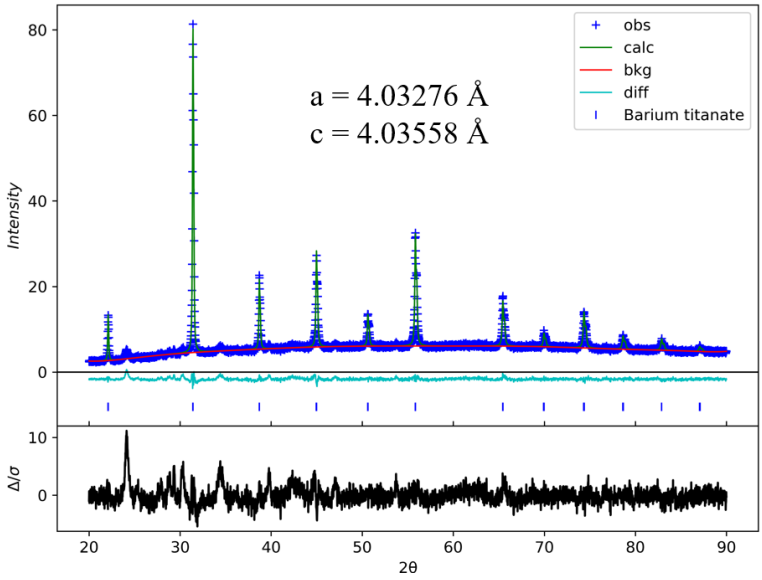

Figure 5.6: Rietveld plot of 2.0 H sample for CaH_2 reduction of synthesised $BaTiO_3$ sample, with tetragonal $BaTiO_3$ as phase reference. Obtained lattice parameters are shown in the Figure.

As can be seen from Figure 5.6, the refinement generates lattice parameters of a = 4.03276 Å, c = 4.03558 Å, further suggesting the formation of a cubic phase. The values are close to each other, and also close to the lattice parameter of a = 4.03376 Å for the 2.0 H sample obtained from refinement with a cubic reference, reported in table 5.3.

The lattice parameters before and after washing, obtained from Rietveld analysis, can be shown in Table 5.3

n_H	Lattice parameter(s) (Å), pre-wash	Lattice parameter(s) (Å), post-wash
0 ($BaTiO_3$)	a = 3.9984(1), c = 4.0257(1)	3.9984(1), c = 4.0257(1)
0.5	4.00891(7)	4.00880(5)
1.0	4.0075(1)	4.00705(7)
1.5	4.0262(2)	4.0269(1)
2.0	4.0333(4)	4.03376(9)

Table 5.3: $BaTiO_{3-x}H_y$ lattice parameters before and after washing for different molar ratios n_H, all heated for 48 hours at 600° C. $BaTiO_3$ wasn't washed.

In agreement with previous research, the lattice parameter increase for higher concentrations of CaH_2 [2]. This is likely due to higher concentrations of CaH_2 leading to greater reduction of the oxides, which increases the abundance of Ti^{3+}. Since Ti^{3+} has a larger ionic radius than Ti^{4+}, this results in an expansion of the lattice parameter. The trend is relatively consistent, with the exception of the $n_H = 1.0$ sample having a smaller lattice parameter then for $n_H = 0.5$. Minor differences between the values before and after washing can be observed, however these are small and considered negligible. The trend of increasing lattice parameters for higher concentrations of CaH_2 can be visualised when plotting lattice parameter against n_H,

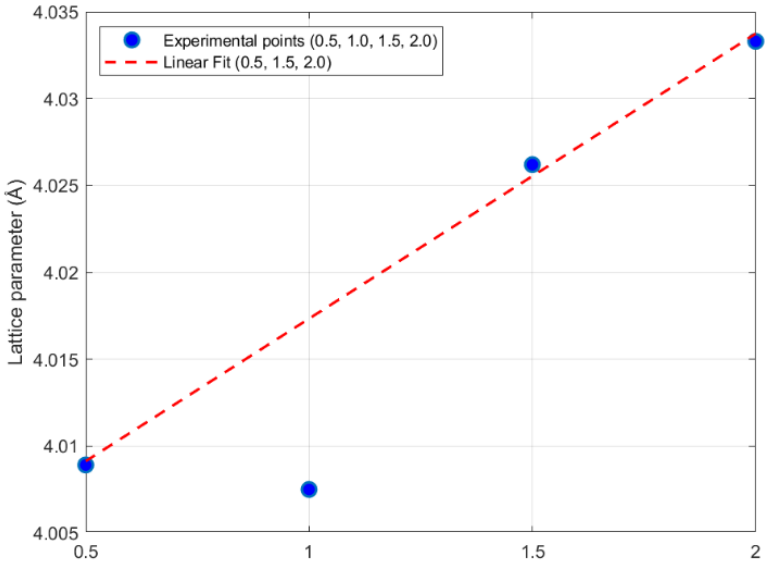

Figure 5.7: Lattice parameter dependence on CaH_2 molar ratio for CaH_2 reduction of synthesised $BaTiO_3$. Linear fit was performed using polyfit function in Matlab.

Looking at Figure 5.7, there is a linear trend if one disregards the 1.0 H sample. However using three data points while omitting one is not definitive. It is likely that for appreciably smaller or larger molar ratios, the data would deviate from this trend. It remains unclear as to why the 1.0 H sample has a smaller lattice parameter than the 0.5 H sample. This result is not expected as higher concentration of metal hydride should reduce $BaTiO_3$ more extensively, as reported from [2]. Nedumkandathil et al. also reports formation of two separate cubic phases, one minority phase

with a slightly larger lattice parameter than that of the majority phase. Two-phase formation should give asymmetry in the peak shape, as two phases of different lattice parameter size will generate two peaks (overlapping). Below is shown the peak shape of the peak around $2\theta = 56^o$ for $n_H = [1.0 ; 2.0]$.

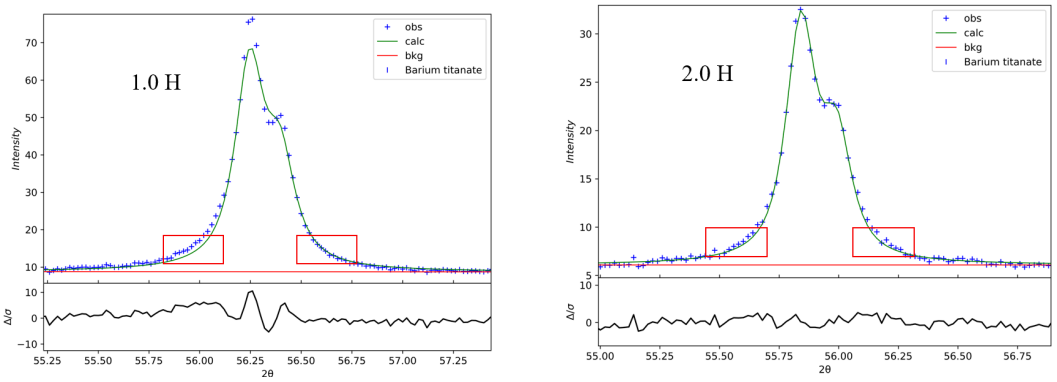

Figure 5.8: Left: Peak shape of 1.0 H CaH_2 reduced $BaTiO_3$ sample. **Right:** Peak shape of 2.0 H CaH_2 reduced $BaTiO_3$ sample. Red rectangles indicate areas of interest.

When performing Rietveld refinement using only one cubic phase as reference, a two-phase formation should become apparent by an asymmetry in the peak shape. In Figure 5.8, the peak shape area of interest is shown with red rectangles. Neither 1.0 H or 2.0 H show any clear suggestions of two phases, as the calculated curve fits the line profile of the experimental data well. However, the 1.0 H sample does show a slight tendency toward what would be expected for multi-phase samples. The calculated fit (green) slightly underestimates the intensity on the left side of the experimental data (blue crosses), compared to the 2.0 H sample where the profile shows near complete symmetry with regards to this. That said, the difference is too small to attribute confidently to the presence of two phases and could instead be explained by uncertainties in the refinement process, or by instrumental and sample effects. Nedumkandathil et al. report much more apparent peak broadening from the additional phase [2]. If an additional phase is present, its weight fraction is likely small. Peaks for samples of 0.5 H and 1.5 H show similar peak shapes to those presented in Figure 5.8. By comparing lattice parameters obtained in table 5.3 with the ones reported from Nedumkandathil et al. in table 2.2, the results suggest that the values obtained are comparative to those of the minority (cubic-II) phase.

All reduced $BaTiO_3$ samples were washed with 0.1M NH_4Cl methanol solution to remove CaO. Before washing, for samples of $n_H = [0.5 ; 1.0 ; 1.5 ; 2.0]$, only CaO and Ba_2TiO_4 were identified as impurities by XRD. Also Ti_3O was identified for the 2.0 H sample. The Ba_2TiO_4 is mainly in orthorhombic phase, while one low intensity peak around $2\theta = 30.3^o$ seems to correspond to the monoclinic phase. For visualisation, XRD patterns for the 2.0 H sample (sample with most intense impurity peaks) before and after washing are shown below.

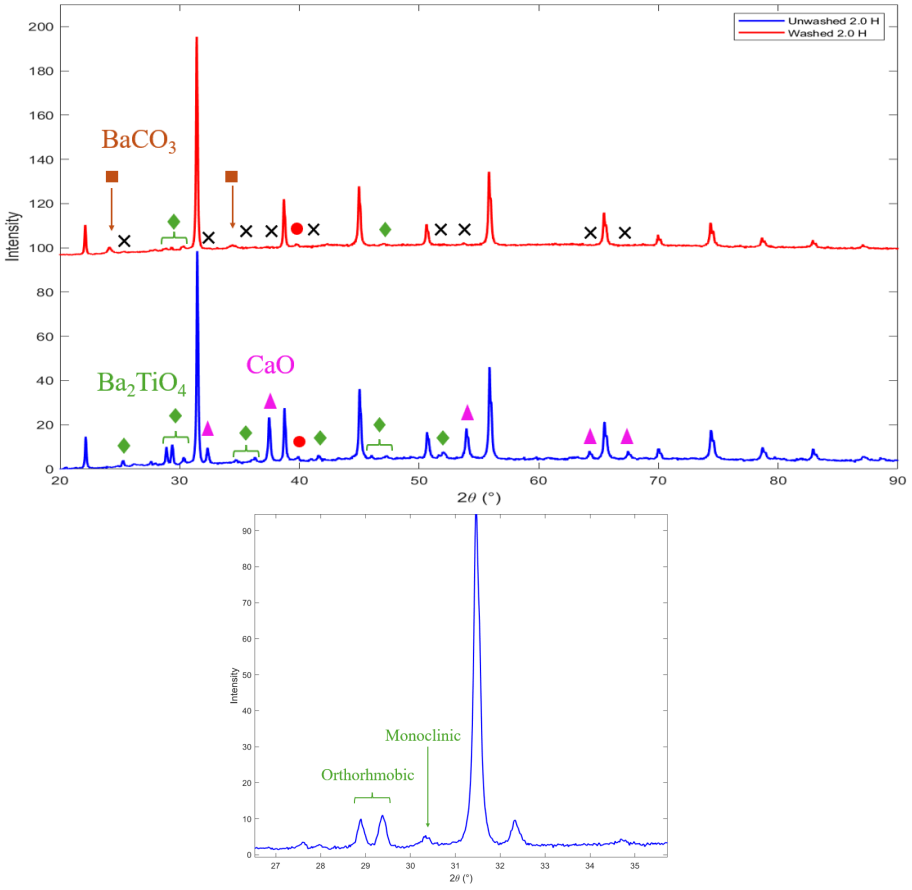

Figure 5.9: Top: XRD patterns for CaH_2 reduced 2.0 H of synthesised $BaTiO_3$ samples before washing (blue curve) and after washing (red curve). Pink triangles, green diamonds, red circles and orange squares show presence of CaO, Ba_2TiO_4 (monoclinic + orthorhombic), Ti_3O and $BaCO_3$ respectively. Black crosses represent eliminated peaks in the XRD pattern. **Bottom:** Peaks for orthorhomic and monoclinic phase of Ba_2TiO_4 in unwashed 2.0 H sample. Images plotted in Matlab.

Figure 5.9 clearly shows an effective removal of CaO, as all CaO diffraction peaks are eliminated after washing. This goes for all samples $n_H = [0.5\ ;\ 1.0\ ;\ 1.5\ ;\ 2.0]$. Amounts of Ba_2TiO_4 (barium orthotitanate) are heavily reduced for all samples, even though some small amounts remain (mainly for the 2.0 H sample). After washing, visible $BaCO_3$ peaks appear for 1.0 H and 2.0 H samples, while 0.5 H and 1.5 H do not show clear signs of $BaCO_3$ formation. Considering Ba_2TiO_4 amounts are reduced and $BaCO_3$ appears, some type of process where Ba_2TiO_4 is converted to $BaCO_3$ is viable. Felgner et al. report of such a process in room temperature with CO_2, in the presence of atmospheric moisture [47].

$$Ba_2TiO_4 + H_2O \rightarrow Ba(OH)_2 + BaTiO_3 \tag{5.1}$$

$$Ba(OH)_2 + CO_2 \rightarrow BaCO_3 \tag{5.2}$$

Marks et al. claim this reaction is possible for both monoclinic and orthorhombic Ba_2TiO_4 [48]. However results from Felgner et al. show that the orthorhombic phase

undergoes this transformation to a greater extent [47]. From Figure 5.9, the two peak intensities around 29^o of the orthorhombic phase are heavily reduced after washing, while the 30.5^o peak of the monoclinic phase remains largely unchanged. These findings are therefore consistent with those reported by Felgner et al [47]. Felgner et al. examined this reaction in air saturated with water vapour for 65 hours, which could provide more favourable reaction conditions. In contrast, it seems unlikely that the same extent of reaction would occur under ambient air during a two-hour methanol washing step. Also, there is no sign of formation of an additional $BaTiO_3$ phase, which the reaction formula suggest.

Amounts of Ba_2TiO_4 impurity seem to significantly increase for higher concentrations of CaH_2.

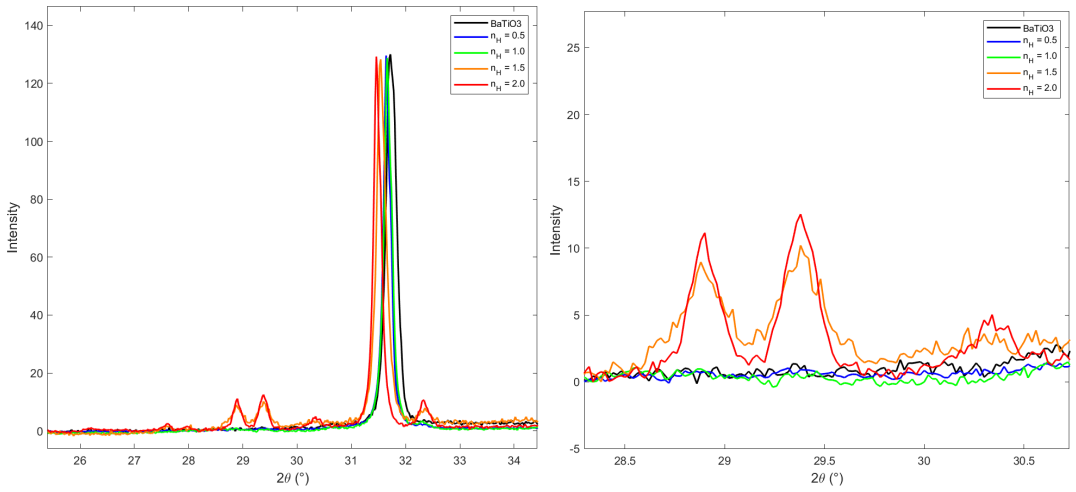

Figure 5.10: Comparison of Ba_2TiO_4 peak intensities around 28.5-30.5^o for reduced synthesised $BaTiO_3$ for different n_H = [0.5 ; 1.0 ; 1.5 ; 2.0]. All peak intensities are normalised to the highest peak around $2\theta = 31.5^o$, and the background level is set uniformly across all patterns. Images plotted in Matlab

Samples of 0.5 H and 1.0 H show noticeably less amounts compared to samples of 1.5 H and 2.0 H, as seen in Figure 5.10. This trend is expected, as more strongly reducing conditions are likely to favour the formation of Ba_2TiO_4. It is likely that the Ti gets over-reduced, leaves the perovskite structure and forms e.g. Ti_3O which formation is confirmed by the peak in Figure 5.9 (marked with red circle). Amounts of Ba_2TiO_4 before washing is not consistent with amounts of $BaCO_3$ formed after washing for the samples of different n_H. For example, the 1.5 H sample has significantly more intense diffraction peaks from Ba_2TiO_4 (seen in Figure 5.10) than the 1.0 H sample, while $BaCO_3$ impurity can only be seen for the 1.0 H sample and not for 1.5 H.

To draw more conclusions concerning the extent of reduction of synthesised $BaTiO_3$ reduced with different molar ratios of CaH_2, TGA measurements are highly relevant. Below is shown TGA curves for respective sample with n_H = [0.5 ; 1.0 ; 1.5 ; 2.0].

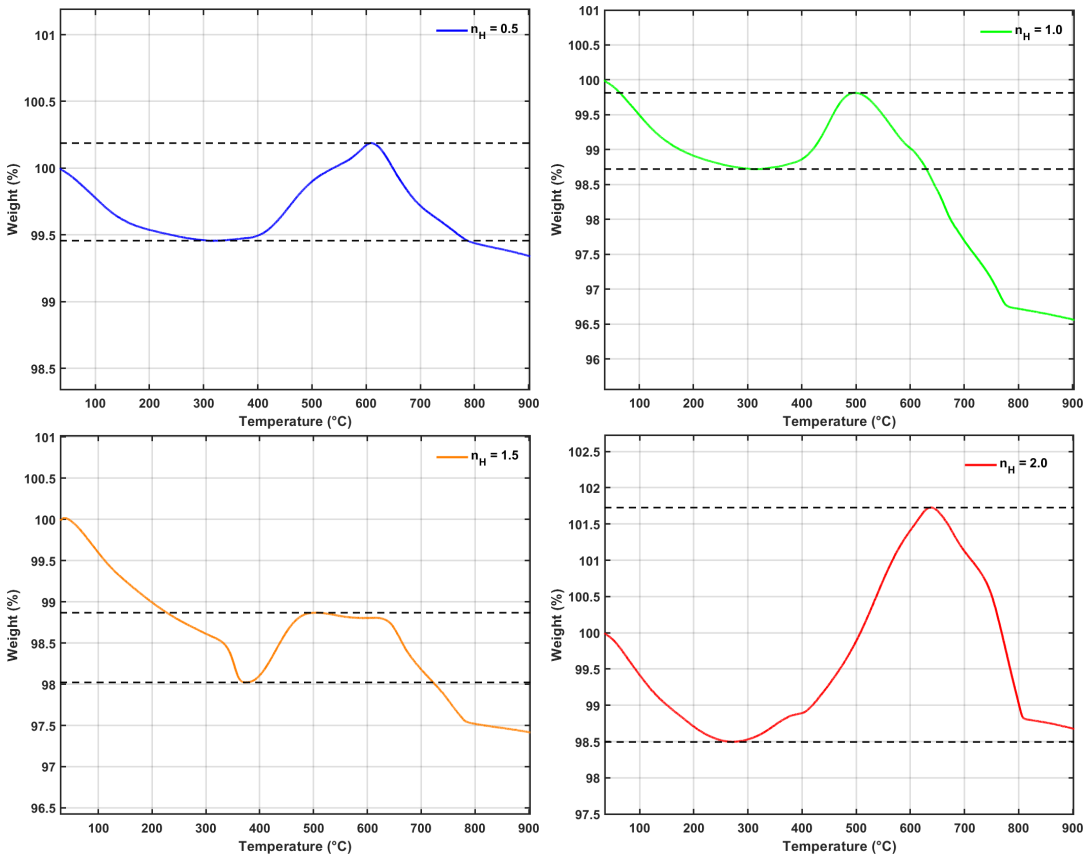

Figure 5.11: TGA data between 35-900° C for products of CaH_2 reduction of $BaTiO_3$ for 48 hours at 600° C for different molar ratios of CaH_2. Black dotted lines correspond to approximate weight difference reference lines before and after oxidation (likely not accurate as discussed below). Images plotted in Matlab.

Generally, the TGA curves in Figure 5.11 show deviation from expected thermal behaviour of the samples. There is a significant weight decrease for all samples around 35-300° C, followed by an expected weight increase caused by oxidation of the reduced $BaTiO_3$ around 350-600° C (different temperature ranges for different CaH_2 concentrations). An additional weight decrease is seen toward the higher temperature range, near 600° C, which seems to stop around 800° C. Some of the mass loss at lower temperatures could be attributed to surface water or possibly remaining methanol evaporating, even though they were vacuum dried before measurement. Any mass loss after oxidation at temperatures over 500-600° C is completely unexpected for $BaTiO_3$, and is likely caused by some decomposition process originating from impurities in the sample. The only impurities confirmed from XRD are $BaCO_3$ and Ba_2TiO_4, where $BaCO_3$ decomposes into BaO and releases CO_2 according to

$$BaCO_3 \rightarrow BaO + CO_2 \tag{5.3}$$

however this decomposition normally occurs at temperatures around 900-1000° C [49]. Also, PXRD diffraction peaks from $BaCO_3$ are not found for all samples, which further suggest that the cause for the mass decrease at high temperatures is not due to $BaCO_3$ decomposition. To gain further knowledge into the features of the TGA

curves, the 2.0 H sample was measured in PXRD after the TGA measurement.

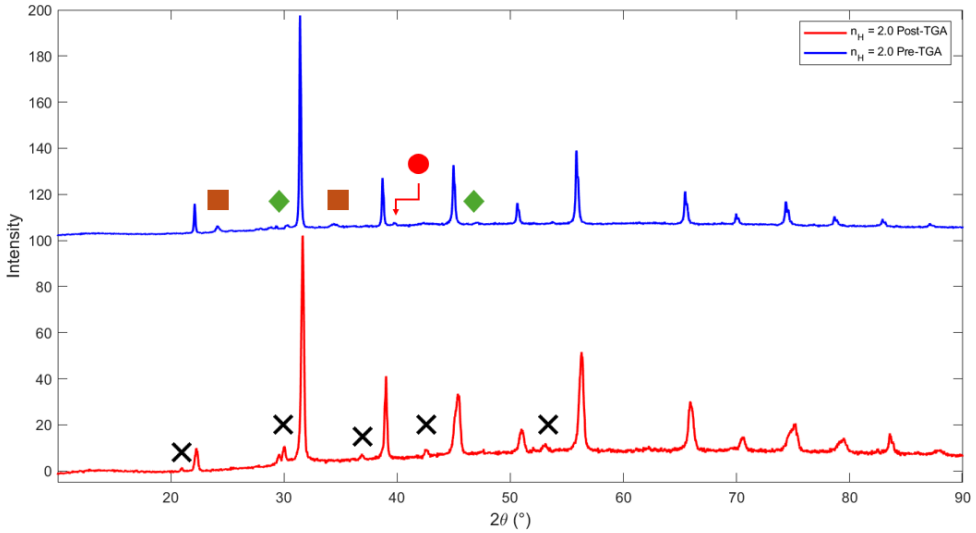

Figure 5.12: XRD patterns for 2.0 H sample of CaH_2 reduced $BaTiO_3$ before (blue) and after (red) TGA measurement. Black crosses represent unidentified phase(s), which peaks only appeared post-TGA. Once again orange squares, green diamonds and red circles represent $BaCO_3$, Ba_2TiO_4 and Ti_3O respectibely. Plotted in Matlab

It is clear from Figure 5.12, that unknown phase(s) are formed during the TGA measurement, suggested by the emergence of new diffraction peaks (shown by the black crosses). This heavily indicates a decomposition process which could explain mass-decreases in the TGA curves. Noticeably, diffraction peaks from $BaCO_3$ and Ti_3O disappear after the measurement, suggesting that these phases undergo some sort of decomposition/reaction. However, the formed impurity phase has not been identified. Multiple Ba–Ti–O phases were considered and compared against databases in EVA software, in spite of this, none of them matched well with the unidentified peaks observed in the post-TGA XRD pattern. It also remains possible that some amorphous impurity, undetectable by XRD, may contribute to the observed mass-decreasing processes. This is especially relevant considering $BaCO_3$, Ba_2TiO_4 and Ti_3O are not identifiable for all molar ratios of CaH_2. From the wider and more asymmetric peaks in the post-TGA XRD pattern (red), it can be confirmed that the reduced perovskite $BaTiO_{3-x}H_y$ is oxidised back to its parent tetragonal $BaTiO_3$ oxide.

The two (or more) mass-decreasing processes cause the quantification of x (in $BaTiO_{3-x}H_y$) to be difficult and unreliable, as they likely overlap with the mass-increasing oxidation step. Yet, x was calculated based on the black-dashed lines in Figure 5.11.

n_H	Lattice parameter (Å)	x from TGA (only vacancies / only hydride ions)
0.5	4.00880(5)	0.106 / 0.113
1.0	4.00705(7)	0.159 / 0.170
1.5	4.0269(1)	0.125 / 0.133
2.0	4.03376(9)	0.463 / 0.494

Table 5.4: Apparent x values for different molar ratios of CaH_2, from products of CaH_2 reduction of $BaTiO_3$. Calculations of x were made considering only oxygen vacancies in the perovskite, as well as only hydride substitution of oxygen. Lattice parameters were included for comparison.

As expected, values of x are not consistent with determined lattice parameters of the samples. In general, a larger lattice parameter is expected to correlate with a higher x value, as both serve as indicators of the extent of reduction, as reported by Nedumkandathil et al. in Table 2.2. For example, the lattice parameter for the 1.5 H sample of 4.0269(1) Å should bring a higher x value compared to the 1.0 H sample with a lattice parameter of 4.00705(7) Å. This is not observed for the obtained values in Table 5.4, where x is higher for 1.0 H ($x \approx 0.16$) compared to 1.5 H ($x \approx 0.13$). As mentioned, the deviating and non-optimal TGA curves give unreliable values of x, causing the lattice parameter to be a better indicator of the degree of reduction. Worth noting however, is the significant reduction of the 2.0 H sample, reflected by high values of both lattice parameter size and x. Samples from attempts of reduction with CaH_2 under H_2 flow showed no colour change, or any indications of reduction from PXRD measurements. Likely, this is due to air not being purged away efficiently in the tube furnace, causing CaH_2 to react with oxygen gas and water in the air instead of reducing $BaTiO_3$.

5.3 Synthesis of nano-$BaTiO_{3-x}H_y$

CaH_2 reduction using manufactured nano-$BaTiO_3$ (cubic phase) was performed to study the impact of $BaTiO_3$ crystallite size in the reduction, while also briefly investigating some effects of heating time and temperature, partially in relation to the Ba_2TiO_4 impurity. All samples presented in this section showed notable colour change from white to dark blue/black, suggesting reduction to some extent.

Firstly, similar to results for synthesised $BaTiO_3$ reduction with CaH_2, two samples with molar ratio $n_H = [1.0 ; 2.0]$ were synthesised. PXRD patterns of these, along with the parent nano-$BaTiO_3$ oxide is shown below.

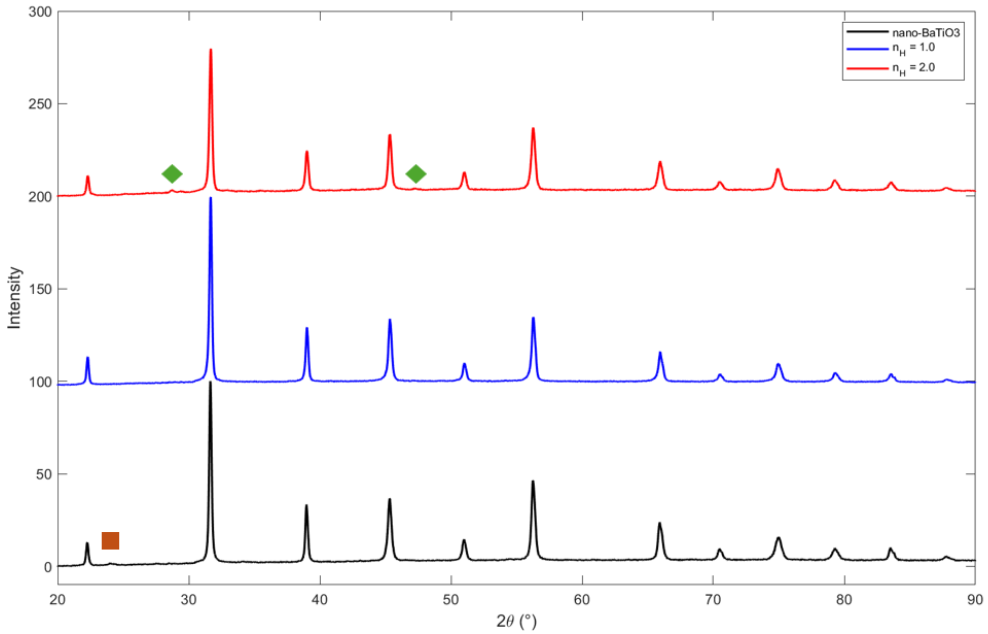

Figure 5.13: PXRD patterns of products from reduction of nano-$BaTiO_3$ for two different concentrations of CaH_2, $n_H = 1.0$ (blue) and $n_H = 2.0$ (red). Orange squares and green diamond symbols represent $BaCO_3$ and Ba_2TiO_4 impurities respectively. Peak intensities are normalised to the most intense peak around $2\theta = 31.5^o$. Measured in variable slit. Plotted in Matlab.

In general there is little difference in the XRD patterns in Figure 5.13, where peak shapes and peak positions are similar for the reduced samples and the oxide. Notable is the $BaCO_3$ impurity for the nano-$BaTiO_3$ oxide, which seem to disappear for the reduced, washed samples of 1.0 H and 2.0 H. From Figure 5.13, quite significant peak broadening can be observed for the perovskite peaks, which is expected from the small crystallite size of nano-$BaTiO_3$. By zooming in on the peaks more closely, this can be examined more closely.

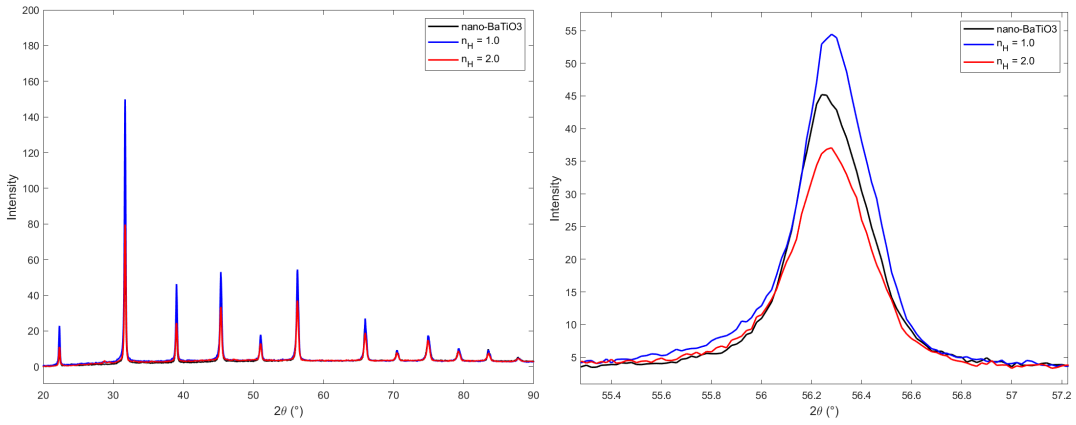

Figure 5.14: Showing of peak broadenings and absence of 2θ shift between the samples peak positions for XRD patterns from reduction of nano-$BaTiO_3$ for two different concentrations of CaH_2, $n_H = 1.0$ (blue) and $n_H = 2.0$ (red). Plotted in Matlab.

As opposed to for CaH_2 reduced samples of synthesised $BaTiO_3$, no apparent 2θ shift trend can be noted from Figure 5.14, suggesting less degree of reduction. To the right in the figure, a zoomed image of the peak around 56.3^o displays the wide peaks obtained from XRD. As mentioned, this is expected due to smaller crystallite size results in fewer number of repeating planes in the crystals, limiting the extent of constructive interference between scattered X-rays [33]. Peak shapes for the samples show little asymmetry, indicating cubic phases for the parent oxide and the reduced samples. Additionally, the label of the industrially manufactured nano-$BaTiO_3$ stated it was in a cubic phase. Initial Rietveld refinements of the samples generated following values of lattice parameters (performed with a cubic reference for all samples, including the oxide).

n_H	Lattice parameter (Å)
0 (nano-$BaTiO_3$)	4.0088(1)
1.0	4.0081(1)
2.0	4.0114(1)

Table 5.5: Lattice parameters for CaH_2 reduced nano-$BaTiO_3$ for $n_H = [1.0 ; 2.0]$, heated at 600° C for 48 hours. Rietveld refinements were performed with a cubic $BaTiO_3$ as reference for the oxide, which is discussed below.

The results from Table 5.3 raised questions. It is unlikely that the 1.0 H reduced sample would have a smaller lattice parameter then that of the unreduced oxide. All reports suggest that a reduction of $BaTiO_3$ should yield a larger lattice parameter, and if the oxide is not reduced at all the lattice parameter should remain unchanged [9, 2]. Hence, a refinement was performed for the nano-$BaTiO_3$ using a tetragonal $BaTiO_3$ phase as reference. Results from this refinement, as well as values for the original cubic refinement are shown in the table below.

Phase of nano-$BaTiO_3$	Lattice parameter(s) (Å)	R_{wp}	χ^2
Cubic	4.0088(1)	5.759 %	2.85
Tetragonal	a = 4.0049(1), c = 4.0180(1)	4.700 %	1.90

Table 5.6: Comparison of lattice parameters and refinement quality indicators for Rietveld refinement of nano-$BaTiO_3$ with cubic and tetragonal reference.

Table 5.6 strongly indicates that the precursor nano-$BaTiO_3$ is in tetragonal phase with a = 4.00493 Å and c = 4.01801 Å. This is shown by the improved refinement quality indicators R_{wp} and χ^2, when performing the refinement with a tetragonal reference. The reason for this not showing in the line profile is likely due to the peak broadening caused by the crystallite size, as the asymmetry is not visible. Rietveld plots are shown for the oxide and samples of $n_H = [1.0 ; 2.0]$ in following figures.

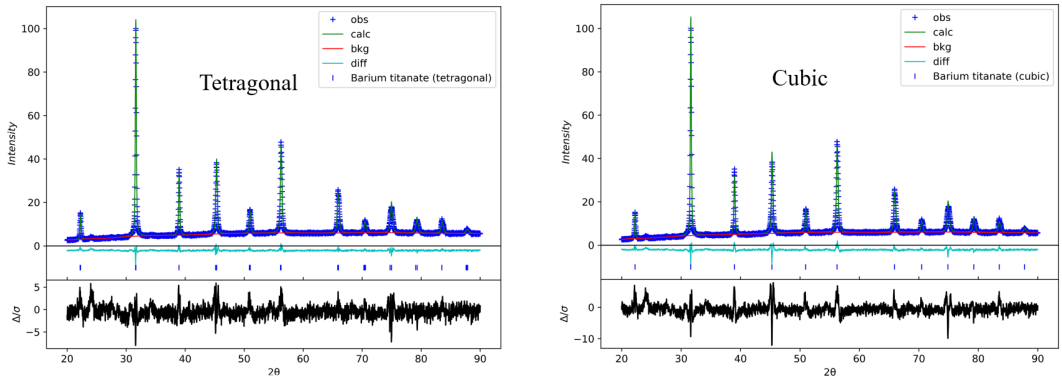

Figure 5.15: Rietveld plots for refinements of nano-$BaTiO_3$, performed with tetragonal reference (left) and cubic reference (right). The blue crosses, green line, and turquoise line correspond to the observed data, calculated fit, and difference curve, respectively

Confirmed from the difference curve (turquoise) in Figure 5.15, tetragonal phase reference generates a better fit.

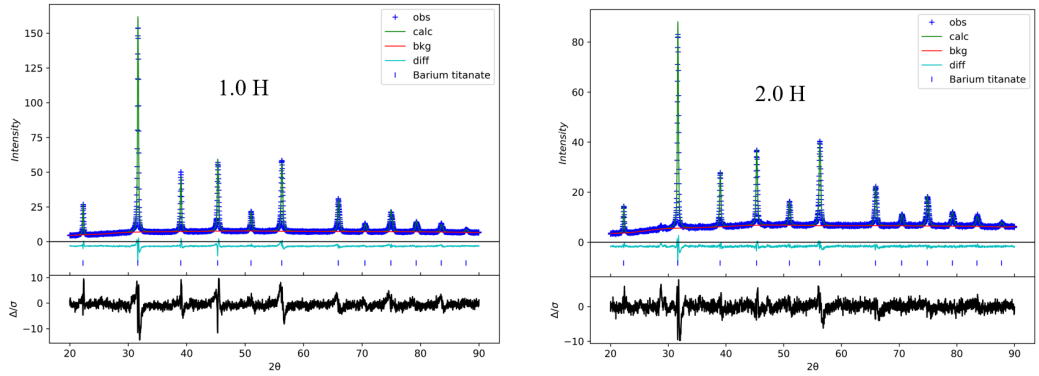

Figure 5.16: Rietveld plots for refinements of products from CaH_2 reduction of nano-$BaTiO_3$ at 600° C for 48 hours, with concentrations of 1.0 H (left) and 2.0 H (right). The blue crosses, green line, and turquoise line correspond to the observed data, calculated fit, and difference curve, respectively.

Obtained lattice parameters from the correct tetragonal refinement in Figure 5.15, as well as for the reduced samples in Figure 5.16 are shown below.

n_H	Lattice parameter(s) (Å)	R_{wp}	χ^2
0 (nano-$BaTiO_3$)	a = 4.0049(1), c = 4.0180(1)	4.700 %	1.90
1.0	4.0081(1)	5.724 %	3.94
2.0	4.0114(1)	4.519 %	2.08

Table 5.7: Lattice parameters and refinement quality indicators for CaH_2 reduced nano-$BaTiO_3$ for n_H = [1.0 ; 2.0], heated at 600° C for 48 hours.

An expected higher lattice parameter for the 2.0 H sample compared to the 1.0 H sample can be seen in Table 5.7. When comparing to previous synthesis results

from from Nedumkandathil et al., the lattice parameter (for 2.0 H primarily), seem to match that of the majority phase reported from [2]. Effects of CaH_2 molar ratio on degree of reduction was explored quite extensively in the result section of synthesised $BaTiO_3$, and is hence not be of focus in this section. Notable however, is that reduction of nano-$BaTiO_3$ seems to be less effected by increased molar ratio of CaH_2, more of which is discussed when comparing nano-$BaTiO_3$ and synthesised $BaTiO_3$.

Two additional samples with molar ratio of $n_H = 2.0$ were synthesised, one with a lower heating time of 24 hours, and one with a lower heating temperature of 580° C. These samples were prepared to provide a limited exploration of the effects of heating time and temperature, in relation to impurity amounts of Ba_2TiO_4 and also to compare the extent of reduction with the original 2.0 H sample (from heating at 600° C for 48 hours). Following figures show PXRD patterns for these three samples.

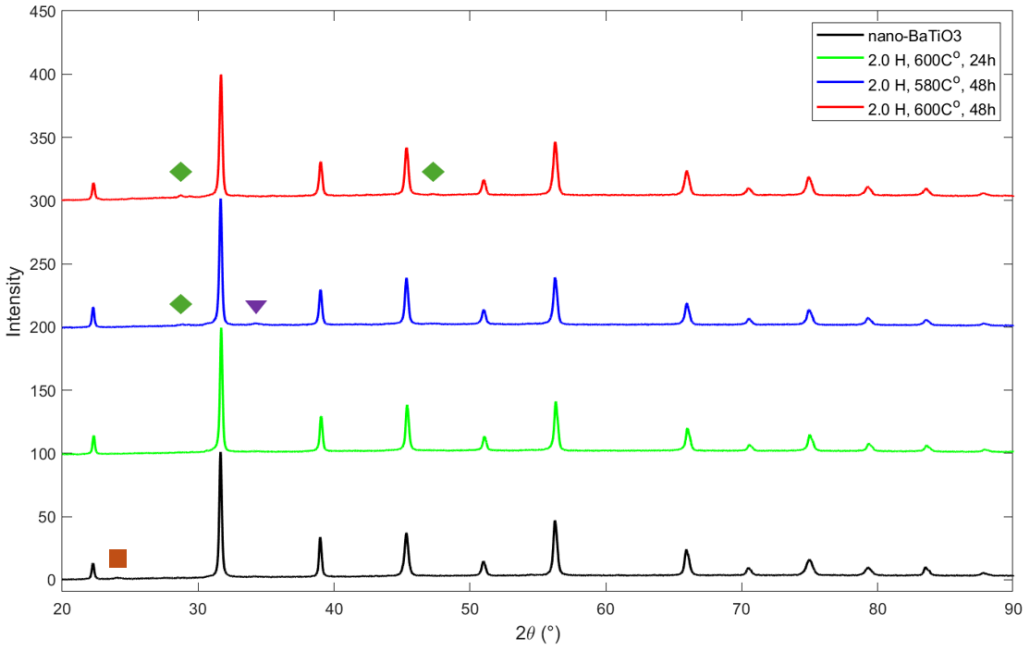

Figure 5.17: PXRD patterns of products from CaH_2 reduction of nano-$BaTiO_3$ with molar ratio $n_H = 2.0$ for different times and temperatures. Orange squares, green diamond symbols and purple upside-down triangles represent $BaCO_3$, Ba_2TiO_4 and $Ca(OH)_2$ impurities respectively. Peak intensities are normalised to the most intense peak around $2\theta = 31.5^o$. Measured in variable slit. Plotted in Matlab.

Like before, no 2θ shift is apparent and peak shapes look similar. A $Ca(OH)_2$ diffraction peak is seen for the 2.0 H sample heated at 580° C for 48 hours. Lattice parameters and refinement quality indicators for the three reduced samples in Figure 5.17 are shown in the table below.

n_H	Temperature (° C)	Time (hours)	Lattice parameter (Å)	R_{wp}	χ^2
2.0	580	48	4.0085(1)	4.900 %	2.93
2.0	600	24	4.0064(1)	4.720 %	2.63
2.0	600	48	4.0114(1)	4.519 %	2.08

Table 5.8: Lattice parameters and refinement quality indicators of products from CaH_2 reduction of nano-$BaTiO_3$ with molar ratio $n_H = 2.0$, for different times and temperatures.

n_H	Temperature (° C)	Time (hours)	Lattice parameter (Å)	R_{wp}	χ^2
1.0	600	48	4.0081(1)	x	x
2.0	580	48	4.0085(1)	4.900 %	2.93
2.0	600	24	4.0064(1)	4.720 %	2.63
2.0	600	48	4.0114(1)	4.519 %	2.08

Table 5.9: Lattice parameters and refinement quality indicators of products from CaH_2 reduction of nano-$BaTiO_3$ with molar ratio $n_H = 2.0$, for different times and temperatures.

By conducting the reduction synthesis for a shorter heating time and at a lower heating temperature respectively, the reaction should yield less reduced products. This can be noted in Table 5.9, where the 2.0 H sample heated at 600° C for 48 hours has the largest lattice parameter. It becomes clear that by heating at 24 hours instead of 48, there is a significant decrease in reduction. This is reflected by the refined lattice parameter of 4.0064(1) Å for the 24 hour sample, compared to the refined lattice parameter of 4.0114(1) Å for the 48 hour sample. Table 5.9 also shows that the reduction is sensitive to temperature, given that a 20^o temperature decrease from 600° C to 580° C lowers the refined lattice parameter from 4.0114(1) Å to 4.0085(1) Å.

The Ba_2TiO_4 impurity was still apparent for the 2.0 H, 48 hour, 600° C sample. The two other experiments were performed with regards to reducing this Ba_2TiO_4 impurity. Meaning that if amounts of impurity doesn't decrease, while lower reduction of the perovskite is obtained, lowering heating temperatures to 580° C or heating times to 24 hours is not meaningful in this specific context. To do this, the samples' PXRD patterns are compared *before* washing, as Ba_2TiO_4 amounts are heavily reduced after the washing step.

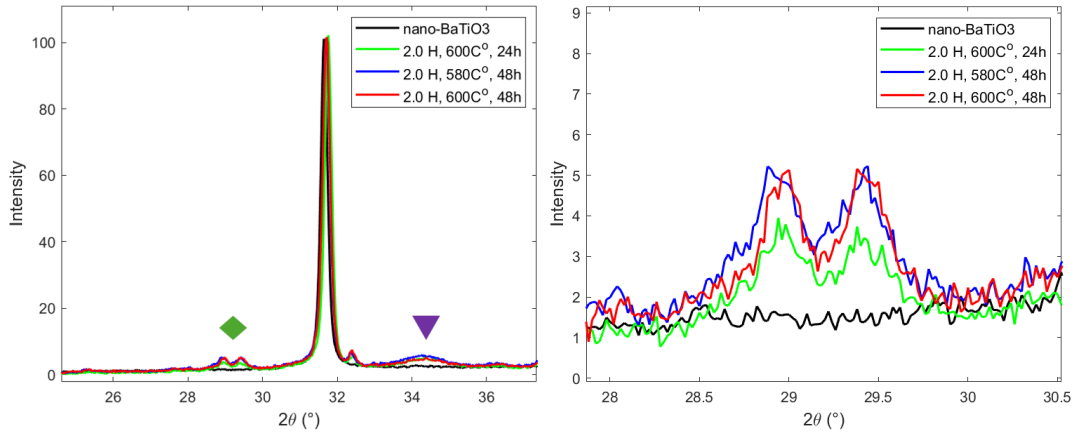

Figure 5.18: Comparison of Ba_2TiO_4 (green diamond symbol) peak intensities around 28.5-30^o for reduced nano-$BaTiO_3$ with molar ratio $n_H = 2.0$ for different times and temperatures, before washing. Purple upside-down triangle correspond to $Ca(OH)_2$ impurities. All peak intensities are normalised to the highest peak around $2\theta = 31.7^o$, and the background level is set uniformly across all patterns. Images plotted in Matlab

In Figure 5.18, 2.0 H samples heated at 580° C and 600° C show near equal amounts of impurity, while exhibiting a difference in lattice parameter size. Lowering the temperature appears to result in a less reduced perovskite phase ($BaTiO_{3-x}H_y$), while not affecting the formation of Ba_2TiO_4. However the comparison of only two temperatures is limited, and the inclusion of additional heating temperatures is needed. The 2.0 H sample heated for 24 hours exhibit a reduction of impurity, noted from the lower intensity of the peaks in the figure. The 24 hour sample was however significantly less reduced (a = 4.0064(1) Å), compared to the sample heated for 48 hours (a = 4.0114(1) Å). Even here, inclusion of more heating times is essential for an extensive analysis and subsequent conclusions. However, the results obtained indicate that neither a temperature nor time decrease are effective alternatives for reducing the Ba_2TiO_4 impurity, while also maintaining the reduction level of the $BaTiO_3$ perovskite phase. Previous results presented in Figure 5.10 show that lower molar concentrations of CaH_2 yields products with no significant amounts of Ba_2TiO_4. These samples also exhibit less reduction based on refined lattice parameters. It would therefore be of interest to investigate whether heating samples of lower molar concentrations for longer times and/or at higher temperatures, yields a more reduced $BaTiO_3$ perovskite, without obtaining Ba_2TiO_4. Before washing, $Ca(OH)_2$ impurity can be seen for all samples, indicated by the purple triangle in Figure 5.18.

Samples of reduced nano-$BaTiO_3$ show asymmetries in the peak shape from Rietveld refinements, visualised in the following figure for two samples.

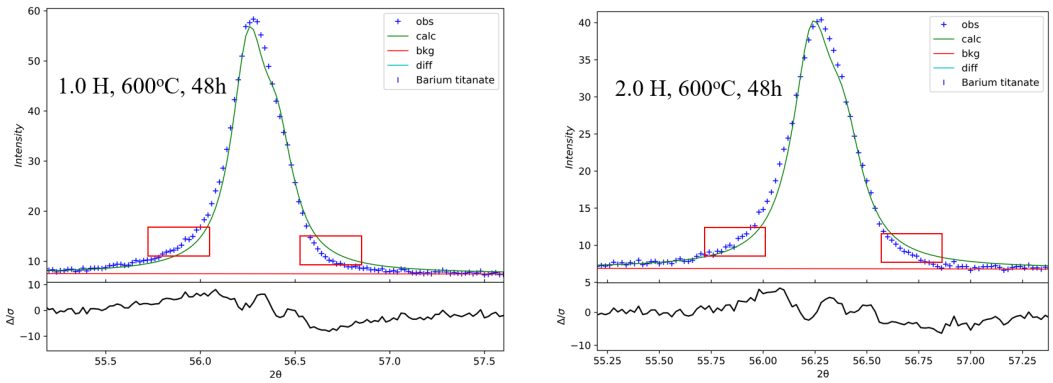

Figure 5.19: Left: Peak shape of refined 1.0 H CaH_2 reduced nano-$BaTiO_3$ sample, heated at 600° C for 48 hours. **Right:** Peak shape of refined 2.0 H CaH_2 reduced nano-$BaTiO_3$ sample, heated at 600° C for 48 hours. Red rectangles indicate areas of interest.

The asymmetry indicated by red rectangles in Figure 5.19 may suggest the presence of two overlapping phases. The calculated fit (green) underestimates the intensity on the left side of the experimental peak (blue crosses) and overestimates it on the right. Such asymmetry can arise from two phases with slightly different lattice parameters and phase fractions, resulting in overlapping diffraction peaks. Since the refinement was performed using a single cubic phase reference, it cannot fully account for this distortion, making two-phase formation a plausible explanation. Originally, it was suspected that this could be due to the larger amounts of precursor used in the nano-$BaTiO_3$ reduction synthesis, compared to the reduction of synthesised $BaTiO_3$. The hypothesis was based on the fact that a larger amount of powder would take up more space in the stainless steel capsule, possibly causing an uneven temperature distribution of the powder in the tube furnace. However, an additional sample was synthesised of the 1.0 H, 600° C, 48 hour sample, using a lesser amount of 0.4 g $BaTiO_3$ as opposed to 1.0 g .

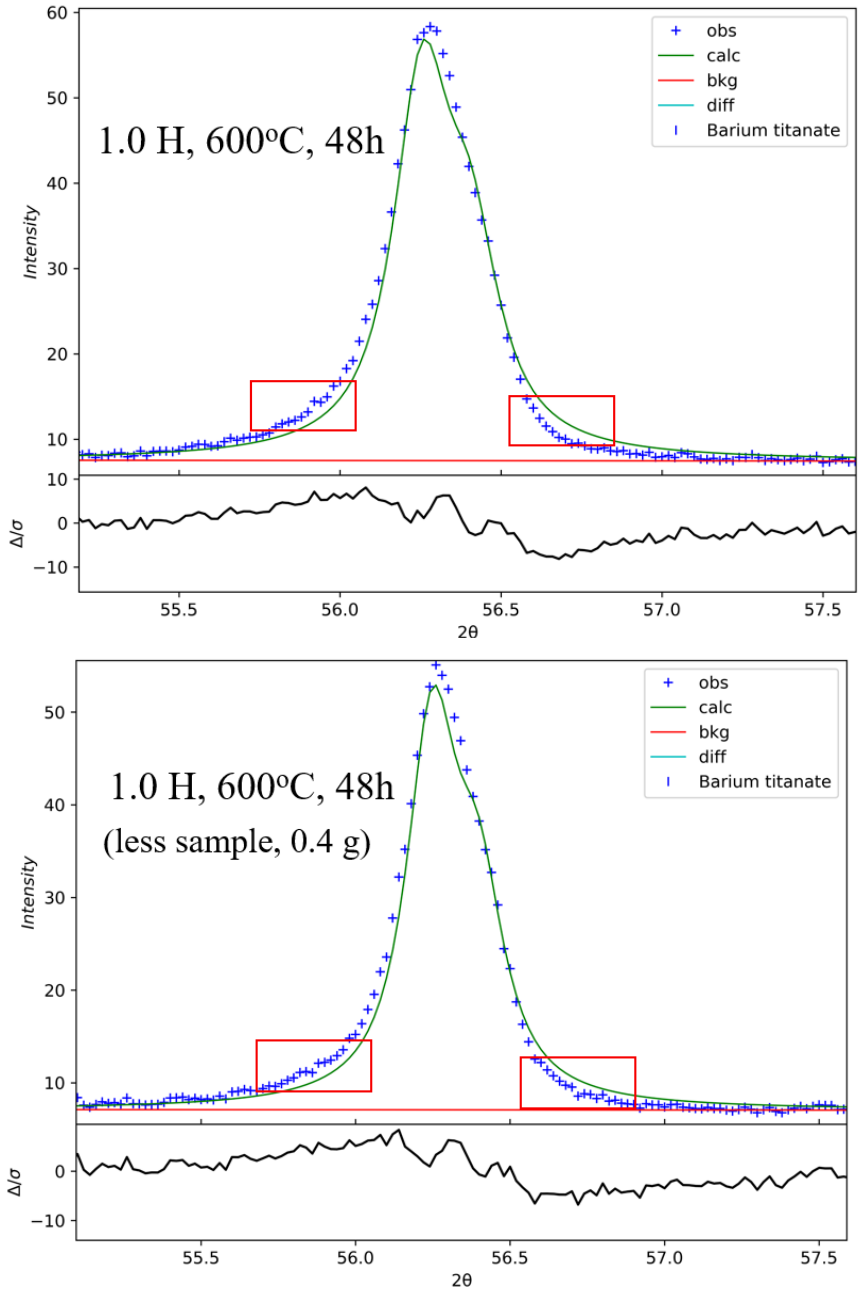

Figure 5.20: Top: Peak shape of refined 1.0 H CaH_2 reduced nano-$BaTiO_3$ sample, heated at 600° C for 48 hours. **Bottom:** Peak shape of refined 1.0 H CaH_2 reduced nano-$BaTiO_3$ sample, heated at 600° C for 48 hours using a smaller precursor amount. Red rectangles indicate areas of interest.

Figure 5.20 clearly shows similar peak shapes, regardless of precursor amounts. This suggests that the higher sample amount isn't a direct cause for the peak asymmetry. The TGA curves for the reduced nano-$BaTiO_3$ exhibit strange and inconclusive behaviour, as illustrated below.

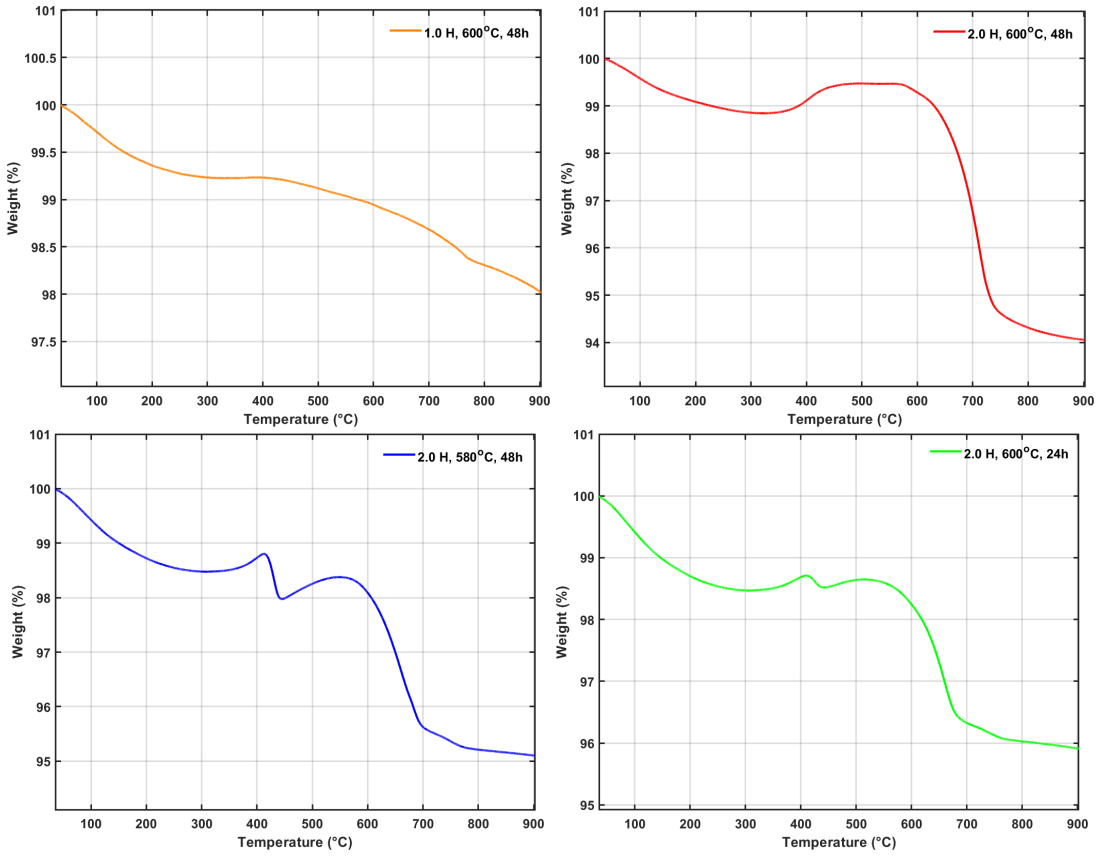

Figure 5.21: TGA curves between 35-900° C for products of CaH_2 reduction of nano-$BaTiO_3$. Images plotted in Matlab.

Looking at the TGA curves in Figure 5.21, they show little sign of reduction. As discussed previously, for the reduction of synthesised $BaTiO_3$, we see a mass decrease in the low temperature range as well as in the high temperature range. This makes the assessment more difficult, since these processes are likely to overlap with the re-oxidation. For the red curve, representing the 2.0 H, 600° C, 48 hour sample, a minimal mass increase from re-oxidation can be noted around 400° C. The 1.0 H sample (yellow curve) exhibit minimal mass increase overall, indicating little reduction.

The blue and green curve, corresponding to 2.0 H, 580° C, 48h and 2.0 H, 600° C, 24h respectively, show very similar behaviour. Notable for these samples, are the mass changes in the 300-550° C temperature region. Initially at 300° C, mass starts to increase, followed by a steep mass decrease just above 400° C, then a slight increase in mass before declining severely after 600° C. The cause of this steep mass decrease is likely due to $Ca(OH)_2$ decomposition to CaO according to

$$Ca(OH)_2 \rightarrow CaO + H_2O(g)$$

which releases water. $Ca(OH)_2$ was identified for the 2.0 H, 580° C, 48h sample in PXRD, and the temperature range for the reaction is relatively consistent with the obtained results. It is likely that the 2.0 H, 600° C, 24h sample also contained $Ca(OH)_2$, despite the absence of detectable diffraction in the PXRD pattern. The mass increases before and after this decomposition suggest that the samples have been reduced to some extent.

5.4 Comparing $BaTiO_{3-x}H_y$ and nano-$BaTiO_{3-x}H_y$

A majority of the results in this subsection have already been presented, but will be presented again to facilitate the comparison of $BaTiO_{3-x}H_y$ and nano-$BaTiO_{3-x}H_y$. Focus is placed on highlighting notable differences in the products obtained from the two different precursor materials.
There is a difference in level of reduction between synthesised and nano-$BaTiO_3$, reflected in obtained lattice parameters, TGA curves and sample colour after reduction. Images of some of the reduced powder samples can be seen below.

Figure 5.22: Image of products from CaH_2 reduction of synthesised (right) and nano-$BaTiO_3$ (left), with molar ratio corresponding to 1.0 H for both samples. Samples heated at 600° C for 48 hours.

As seen in Figure 5.22, 1.0 H sample of reduced synthesised $BaTiO_3$ show a darker blue/almost black colour, while a notably lighter blue colour is noted for the 1.0 H sample of reduced nano-$BaTiO_3$. A darker blue/black colour indicates a higher extent of reduction [9]. This is also observed through the lattice parameters obtained from Rietveld refinement, especially for higher molar ratios of CaH_2.

n_H	Lattice parameter(s), synthesised (Å)	Lattice parameter(s), nano (Å)
0 ($BaTiO_3$)	a = 3.9984(1), c = 4.0257(1)	a = 4.0049(1), c = 4.0180(1)
0.5	4.00891(7)	x
1.0	4.00705(7)	4.0081(1)
1.5	4.0269(1)	x
2.0	4.03376(9)	4.0114(1)

Table 5.10: Lattice parameters for products of CaH_2 reduction of synthesised and nano-$BaTiO_3$ for different molar ratios of CaH_2, heated at 600° C for 48 hours. No samples of 0.5 H and 1.5 H were synthesised for nano-$BaTiO_3$.

Looking at Table 5.10, the precursor oxides differ in lattice parameters a and c, which will effect the lattice parameters obtained for the reduced samples. Generally

however, samples of reduced, synthesised $BaTiO_3$ obtain higher lattice parameters then those of the reduced nano-$BaTiO_3$. For example, samples of 1.5 H and 2.0 H of synthesised $BaTiO_3$ have significantly larger lattice parameters then the 2.0 H sample of nano-$BaTiO_3$, indicating higher extent of reduction for synthesised $BaTiO_3$. This is further suggested and confirmed by the TGA curves, comparing samples of 1.0 H and 2.0 H.

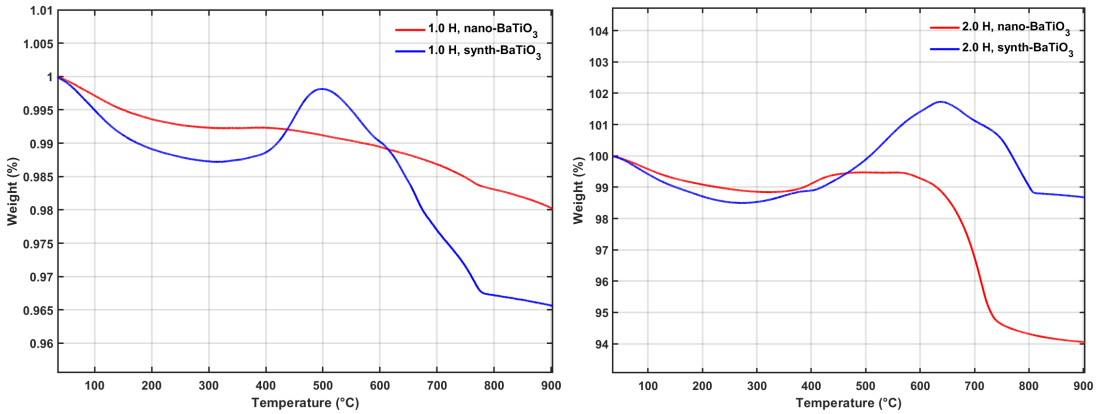

Figure 5.23: Left: TGA curves for samples of 1.0 H, heated at 600° C for 48 hours of CaH_2 reduced nano-$BaTiO_3$ (red) and synthesised $BaTiO_3$ (blue). **Right:** TGA curves for samples of 2.0 H, heated at 600° C for 48 hours of CaH_2 reduced nano-$BaTiO_3$ (red) and synthesised $BaTiO_3$ (blue).

TGA curves in Figure 5.23 clearly indicates higher reduction for samples of synthesised $BaTiO_3$, exhibiting much bigger mass differences in the re-oxidation step. As mentioned, the TGA curves for reduced samples of nano-$BaTiO_3$ barely exhibit any re-oxidation at all, particularly not for the 1.0 H sample. These results were not expected, as the natural higher surface area of nano-crystalline $BaTiO_3$ was expected to facilitate the CaH_2 reduction. More precursor amounts were used for the synthesis with nano-powder, which could potentially lower reduction. However the nano-$BaTiO_3$ sample of 1.0 H, using same precursor amount as for synthesised $BaTiO_3$ (0.4 g), didn't show signs of higher reduction.

n_H / $BaTiO_3$ amount (g)	Lattice parameter (Å)
1.0 / 0.4	4.0076(1)
1.0 / 1.0	4.0081(1)

Table 5.11: Lattice parameters for CaH_2 reduced nano-$BaTiO_3$ for $n_H = 1.0$ with different precursor amounts of nano-$BaTiO_3$, heated at 600° C for 48 hours.

Table 5.11 show no significant change in lattice parameter for smaller precursor amounts, indicating roughly same extent of reduction for both samples. It would be of interest to examine this for samples of 2.0 H also.
Samples of CaH_2 reduced nano-$BaTiO_3$ show stronger indications of two-phase formation, indicated by a larger asymmetry in the Rietveld fit of the peak shapes.

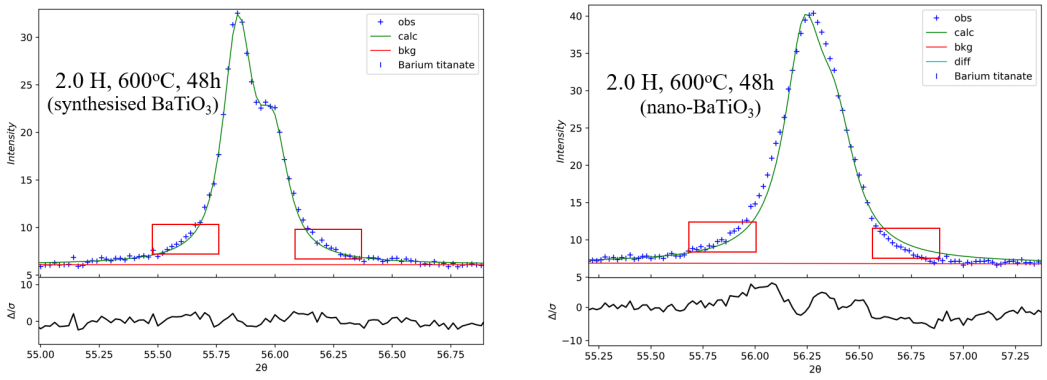

Figure 5.24: Left: Peak shape of refined 2.0 H CaH_2 reduced synthesised $BaTiO_3$ sample, heated at 600° C for 48 hours. **Right:** Peak shape of refined 2.0 H CaH_2 reduced nano-$BaTiO_3$ sample, heated at 600° C for 48 hours. Red rectangles indicate areas of interest.

As seen in Figure 5.24, the 2.0 H sample of nano-$BaTiO_3$ exhibits larger asymmetries in the line profiles, while the calculated curve for the 2.0 H sample of synthesised $BaTiO_3$ fits the data more accurately in this region (indicated by red rectangles). Even though not confirmed, this could indicate a similar two-phase formation for the nano sample, as reported from Nedumkandathil et al [2]. To further investigate this, it would be beneficial to perform Rietveld refinements with two cubic reference phases.

5.5 Synthesis of $BaZr_{0.5}In_{0.5}O_{2.75}$ and $BaZr_{0.5}In_{0.5}O_{2.75-x}H_y$

The confirmation of formation of the perovskite barium indate-zirconate oxide (BZO) is perhaps not as reliable as for $BaTiO_3$, considering there is not a reported CIF file reference for the specific oxide. Chemical analysis of all samples would be beneficial to determine indium and zirconium content. However, by comparing with a $BaZrO_3$ perovskite reference while considering that equal amounts of In_2O_3 and $BaZrO_3$ were used, the BZO perovskite oxide formation can be supported. The image below, extracted from EVA software, visualises this.

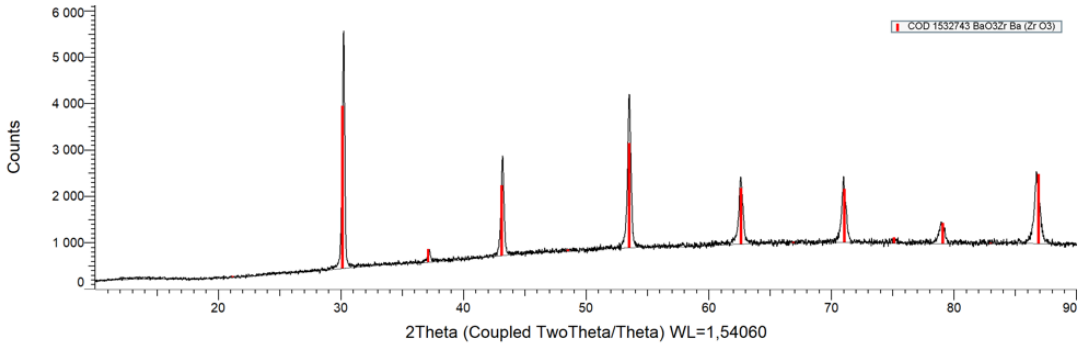

Figure 5.25: PXRD pattern of synthesised 50% BZO, with vertical reference lines of $BaZrO_3$ in red. COD ID: 1532743. Image extracted from EVA software.

A successful perovskite formation can be noted in Figure 5.25, likely with indium inclusion as no impurity diffraction peaks are seen. A slight peak shift toward lower angles at higher 2θ can be seen for the synthesised BZO, compared to the $BaZrO_3$ reference. At lower 2θ the peaks match more symmetrically, which could be an indication of indium inclusion as In(III) has a larger ionic radius compared to Zr(IV) in an octahedral coordination [50]. Indium inclusion could hence increase lattice parameter, which would shift the peaks toward lower angles at higher 2θ. Presence of amorphous impurities is possible, as the background noise increases quite substantially for higher 2θ angles.

The results analysis of oxyhydrides of barium indate-zirconate (BZOH) will be more reliant on TGA curves in order to determine how much reduction has occured, as there isn't a significant lattice parameter change, such as for reduction of $BaTiO_3$ [12]. PXRD patterns of the 50% indium substituted BZO and BZOH are shown in the following figure.

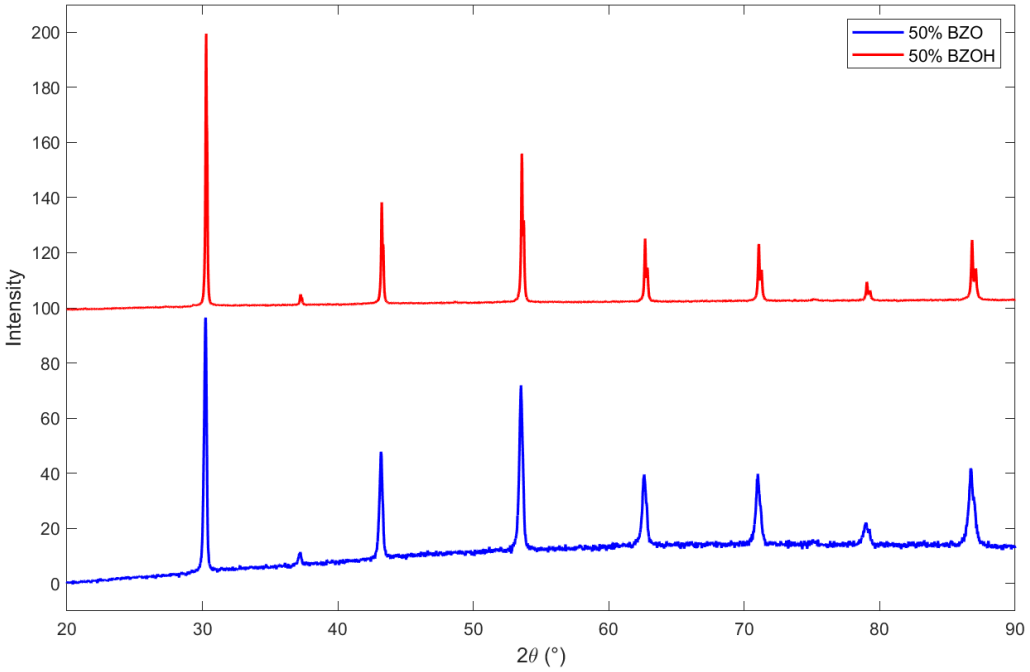

Figure 5.26: PXRD pattern of synthesised 50% BZO (blue) and H_2 reduced 50% BZOH (red). BZOH sample heated at 800° C for 24 hours, with 8 ml/min H_2 flow. Peak intensities are normalised to the highest intensity peak. Plotted in Matlab.

Figure 5.26 shows clearly that the perovskite peaks are intact after H_2 reduction. The background noise for higher angles appears to disappear, and the peaks exhibit increased sharpness and resolution for the reduced sample. As mentioned, determining the degree of reduction will heavily rely on the TGA curve, shown below.

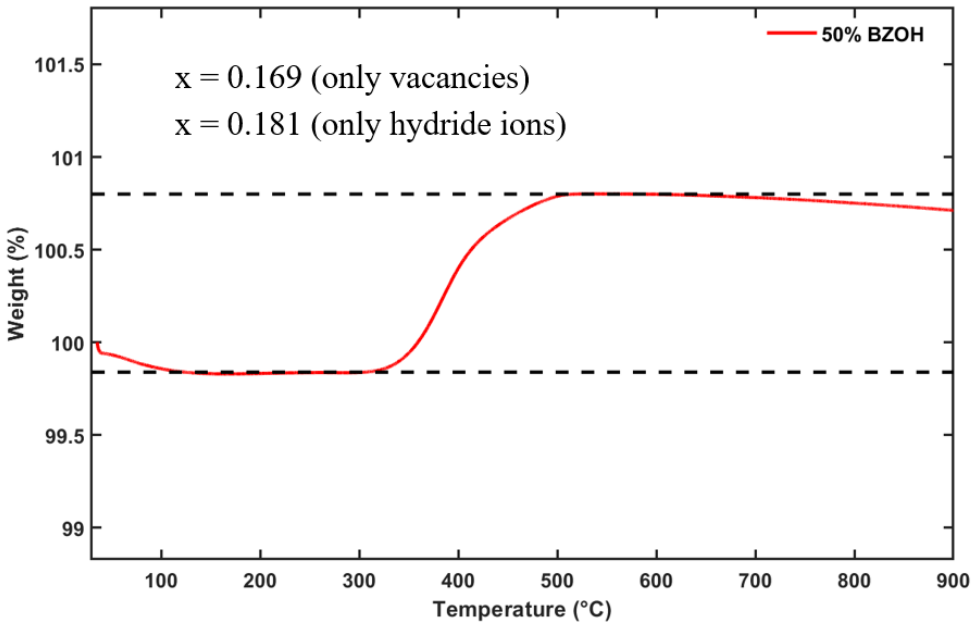

Figure 5.27: TGA curves between 35-900° C for 50% BZOH sample. Reported x values for $BaZr_{0.5}In_{0.5}O_{2.75-x}H_y$ are shown, assuming vacancy formation as well as hydride incorporation only. Plotted in Matlab.

The thermal behaviour of 50% BZOH, represented by the TGA curve in Figure 5.27, show promising characteristics. The sample exhibits a constant mass in the region between around 100-310° C, followed by a mass increasing re-oxidation step of the reduced perovskite in the temperature range of around 320-510° C, after which the mass remains constant up to above 600° C. This behaviour allows for a reliable determination of x, and confirms reduction of the 50% BZO oxide. The reduction is less significant compared to results from Toriumi et al., where they give reports of $x = 0.44$ [12], compared to the obtained value in Figure 5.27 of $x = 0.169$-0.181. The TGA measurements give no information regarding H^- incorporation in the perovskite. For this, inelastic neutron scattering (INS) can be utilized.

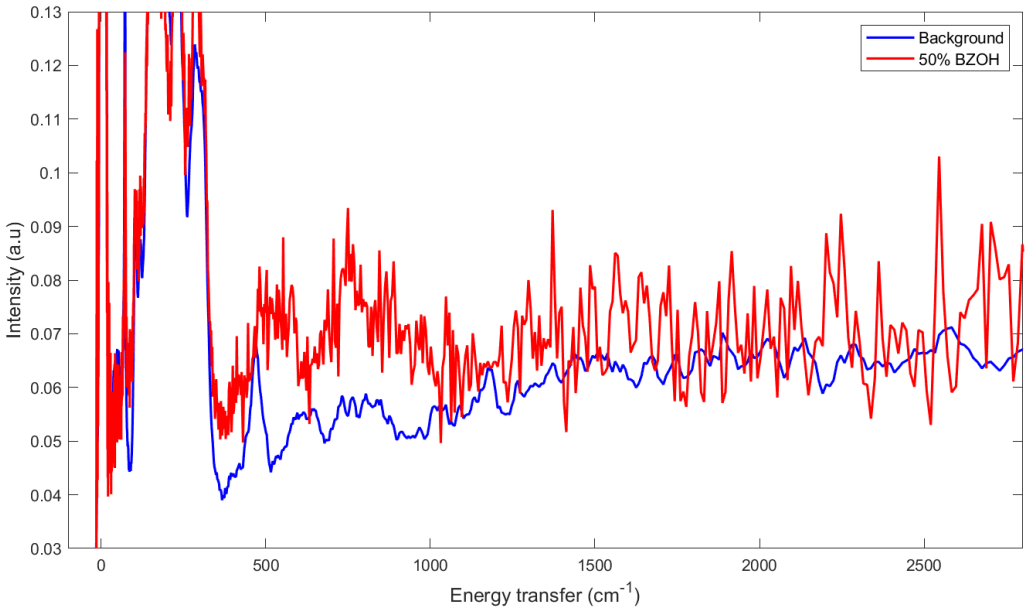

Figure 5.28: Back-scattering INS spectrum for 50% BZOH sample (red). Background measurement is shown in blue. Plotted in Matlab.

Figure 5.28 reveals that, quite unexpectedly, little hydride incorporation has occurred for the 50% BZOH sample. Reduction is clearly shown from the TGA curve, however as opposed to results from Toriami et al., this reduction seem to correspond almost exclusively to oxygen vacancy formation. If a substantial amount of H^- ions were present in the sample, one would expect to observe prominent, high-intensity vibrational peaks in the range shown in Figure 5.28. Considering the prominent reduction shown in Figure 5.27, and more or less equal synthesis procedures as from [12], which report formation of oxyhydride $BaZr_{0.5}In_{0.5}O_{2.25}H_{0.5}$, these results are surprising.

5.6 Synthesis of $BaZr_{0.3}In_{0.7}O_{2.65}$ and $BaZr_{0.3}In_{0.7}O_{2.65-x}H_y$

The 70% doped barium-indate zirconate oxide (70% BZO) is compared to a $BaZrO_3$ reference, in the same way as for 50% BZO, to support the formation of the per-

ovskite oxide. PXRD pattern of 70% BZO with $BaZrO_3$ reference is shown below.

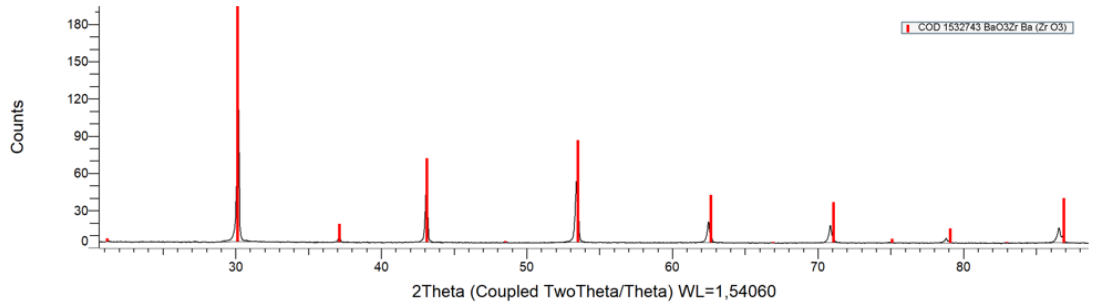

Figure 5.29: PXRD pattern of synthesised 70% BZO, with vertical reference lines of $BaZrO_3$ in red. COD ID: 1532743. Image extracted from EVA software.

Also in Figure 5.29 we note a successful perovskite formation, with a more declared shifting of the peaks to the left at higher 2θ angles, suggesting a richer inclusion of In(III) for the 70% BZO sample compared to the 50% BZO (which is expected). The overall background is also significantly smaller across the entire PXRD pattern, exhibiting no signs of amorphous impurities. No apparent impurity diffraction peaks are seen either. PXRD patterns of 70% BZO and BZOH are shown in the following figure.

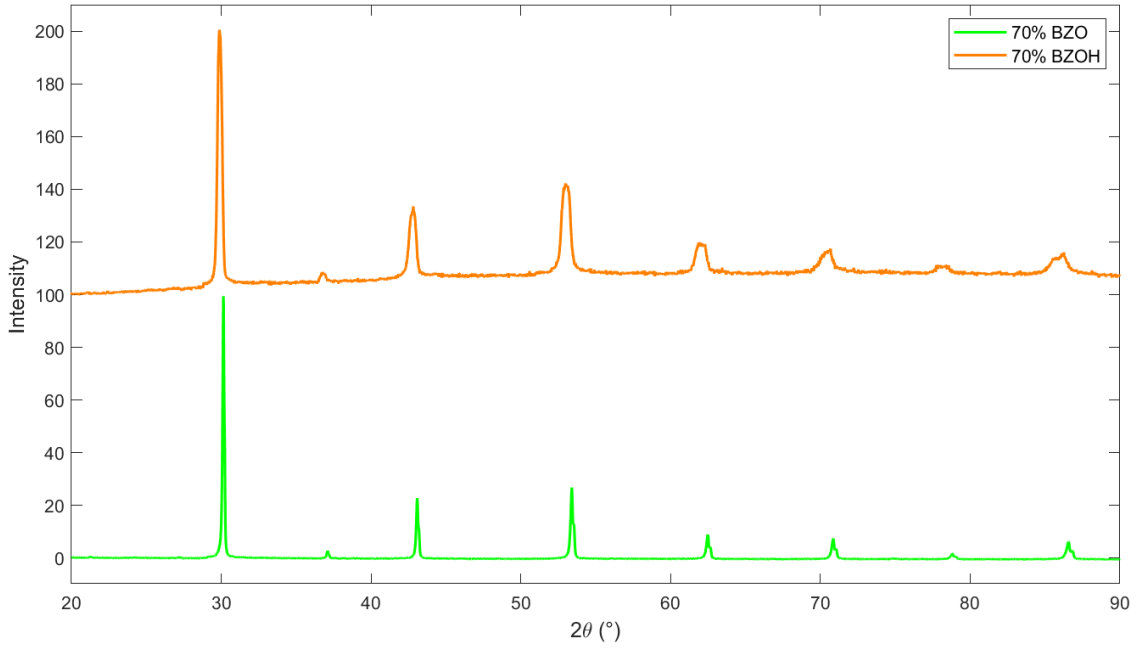

Figure 5.30: PXRD pattern of synthesised 70% BZO (green) and H_2 reduced 70% BZOH (orange). BZOH sample heated at 650° C for 20 hours, with 8 ml/min H_2 flow. Peak intensities are normalised to the highest intensity peak. Plotted in Matlab.

In Figure 5.30, the 70% BZO and BZOH exhibit a different behaviour as opposed to the 50% BZO and BZOH. The peaks of the reduced 70% BZOH are more broadened

and show differences in peak shape, compared to the peaks of oxide. Additionally, BZOH diffraction peaks are shifted to the left. These observations could be attributed to changes in the material after H_2 reduction, such as lattice strain and expansion. Toriumi et al. report of a slight lattice contraction, with lattice parameter decreasing from 4.2020 to 4.1990 Å after H_2 reduction, inconsistent with an eventual lattice expansion for 70% BZOH results. To further examine this, the TGA curve for reduced 70% BZOH is needed.

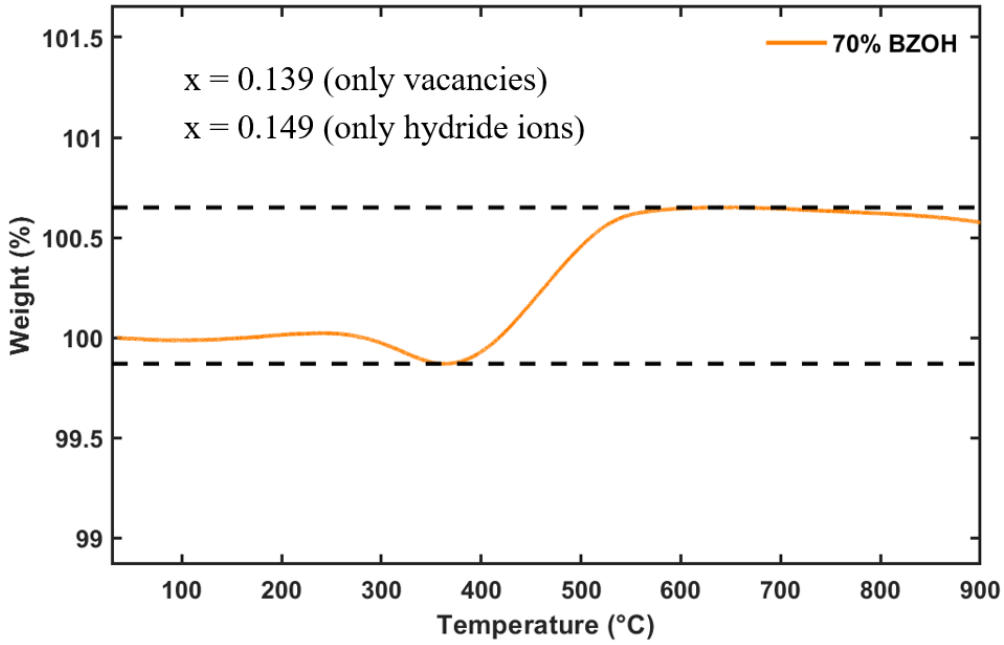

Figure 5.31: TGA curves between 35-900° C for 70% BZOH sample. Reported x values for $BaZr_{0.3}In_{0.7}O_{2.65-x}H_y$ are shown, assuming vacancy formation as well as hydride incorporation only. Plotted in Matlab.

The thermal behaviour of 70% BZOH, illustrated by the TGA curve in Figure 5.31, displays similar characteristics to that of the 50% sample. After an initial stable region up to approximately 280° C, a minor mass decrease is observed just before the re-oxidation onset, which is not seen for the 50% BZOH. This is followed by a mass-gaining step corresponding to the re-oxidation of the reduced perovskite in the temperature range of roughly 350–550° C. Beyond this, the mass remains stable up to above 600° C. This behaviour supports a determination of x and confirms reduction of the 70% BZO oxide. The degree of reduction is, once again, lower than that reported by Toriumi et al. (x = 0.44 [12]), with an obtained value in Figure 5.31 of x = 0.139–0.149. The 70% BZOH sample is slightly less reduced than the 50% sample, as indicated by the lower x values. This suggests a smaller extent of reduction, however the values are comparable. As with the 50% sample, TGA alone does not reveal whether H^- has been incorporated into the perovskite lattice. Considering the 50% BZOH didn't show significant hydride incorporation, a similar result could be likely for the 70% BZOH, though this remains speculative.

6
Conclusions

The most important and concrete results from chapter 5 will briefly be summarised in this chapter.
To conclude, the results of the thesis show

i. CaH_2 reduction of synthesised tetragonal $BaTiO_3$ at 600° C for 48 hours give reduced products of cubic phase where the color changes from white to black-/dark blue. Results generally show that a higher molar ratio of CaH_2 leads to a higher degree of reduction.
ii. Rietveld refinements of reduced samples of synthesised $BaTiO_3$ at 600° C for 48 hours exhibit single-phase formation.
iii. CaH_2 reduction of nano-$BaTiO_3$ at 600° C for 48 hours yields a less reduced perovskite phase compared to for synthesised $BaTiO_3$.
iv. Rietveld refinements of reduced samples of nano-$BaTiO_3$ at 600° C for 48 hours show heavier indications to two-phase formation, compared to the reduced samples of synthesised $BaTiO_3$.
v. Particularly for higher molar ratios of CaH_2, substantial amounts of a barium orthotitanate, Ba_2TiO_4, phase are found for both reduced products of synthesised $BaTiO_3$ and nano-$BaTiO_3$. Quantities of this impurity significantly decrease for lower molar ratios of CaH_2. A temperature decrease to 580° C didn't decrease Ba_2TiO_4 amounts, while a heating time of 24 hours lead to decreased amounts, however not without affecting the degree of reduction for the $BaTiO_3$ perovskite phase considerably.
vi. H_2 annealing of the 50% substituted BZO at 800° C for 24 hours, and the 70% substituted BZO at 650° C for 20 hours, yielded reduced perovskite oxides BZOH. Extent of reduction was comparable for both BZOH samples.
vii. INS measurements showed minimal hydride incorporation for the 50% BZOH.

Bibliography

[1] Momma K, Izumi F. VESTA 3 for three-dimensional visualization of crystal, volumetric and morphology data. Journal of Applied Crystallography. 2011;44(6):1272-6. Available from: https://journals.iucr.org/paper?db5098https://journals.iucr.org/j/issues/2011/06/00/db5098/.

[2] Nedumkandathil R, Jaworski A, Grins J, Bernin D, Karlsson M, Eklöf-Österberg C, et al. Hydride Reduction of $BaTiO_3$? Oxyhydride Versus O Vacancy Formation. ACS Omega. 2018 9;3(9):11426-38.

[3] Lam E, Corral-Pérez JJ, Larmier K, Noh G, Wolf P, Comas-Vives A, et al. CO_2 Hydrogenation on Cu/Al_2O_3 : Role of the Metal/Support Interface in Driving Activity and Selectivity of a Bifunctional Catalyst . Angewandte Chemie. 2019 9;131(39):14127-34.

[4] Li K, Chen JG. CO_2 Hydrogenation to Methanol over ZrO_2-Containing Catalysts: Insights into ZrO_2 Induced Synergy. ACS Catalysis. 2019 9;9(9):7840-61.

[5] Tian G, Li Z, Zhang C, Liu X, Fan X, Shen K, et al. Upgrading CO_2 to sustainable aromatics via perovskite-mediated tandem catalysis. Nature communications. 2024 12;15(1):3037.

[6] Khdary NH, Alayyar AS, Alsarhan LM, Alshihri S, Mokhtar M. Metal Oxides as Catalyst/Supporter for CO_2 Capture and Conversion, Review. MDPI; 2022.

[7] Qin Z, Ren J, Miao M, Li Z, Lin J, Xie K. The catalytic methanation of coke oven gas over Ni-Ce/Al_2O_3 catalysts prepared by microwave heating: Effect of amorphous NiO formation. Applied Catalysis B: Environmental. 2015 3;164:18-30. Available from: https://www.sciencedirect.com/science/article/abs/pii/S0926337314005256?via%3Dihub.

[8] He Y, Li Y, Lei M, Polo-Garzon F, Perez-Aguilar J, Bare SR, et al. Significant Roles of Surface Hydrides in Enhancing the Performance of $Cu/BaTiO_{2.8}H_{0.2}$ Catalyst for CO_2 Hydrogenation to Methanol. Angewandte Chemie - International Edition. 2024 1;63(1).

[9] Kobayashi Y, Hernandez OJ, Sakaguchi T, Yajima T, Roisnel T, Tsujimoto Y, et al. An oxyhydride of $BaTiO_3$ exhibiting hydride exchange and electronic conductivity. Nature Materials. 2012;11(6):507-11.

[10] Jiang Y, Takashima R, Nakao T, Miyazaki M, Lu Y, Sasase M, et al. Boosted Activity of Cobalt Catalysts for Ammonia Synthesis with $BaAl_2O_{4-x}H_y$ Electrides. Journal of the American Chemical Society. 2023 5;145(19):10669-80.

[11] Iwazaki Y, Suzuki T, Mizuno Y, Tsuneyuki S. Doping-induced phase transitions in ferroelectric $BaTiO_3$ from first-principles calculations. Physical Review B - Condensed Matter and Materials Physics. 2012 12;86(21).

[12] Toriumi H, Kobayashi G, Saito T, Kamiyama T, Sakai T, Nomura T, et al. Barium Indate-Zirconate Perovskite Oxyhydride with Enhanced Hydride Ion/-Electron Mixed Conductivity. Chemistry of Materials. 2022 8;34(16):7389-401.

[13] Kobayashi Y, Hernandez O, Tassel C, Kageyama H. New chemistry of transition metal oxyhydrides. Taylor and Francis Ltd.; 2017.

[14] Uchimura T, Takeiri F, Okamoto K, Saito T, Kamiyama T, Kobayashi G. Direct synthesis of barium titanium oxyhydride for use as a hydrogen permeable electrode. Journal of Materials Chemistry A. 2021 9;9(36):20371-4.

[15] Huang B, Corbett J. . Journal of Solid State Chemistry. 1998;141:570 -575.

[16] Fokin V, Malov Y, Fokina E, Troitskaya S, Shilkin S. . International Journal of Hydrogen Energy. 1995;20:387 -389.

[17] Eklof-Osterberg C. Structure-dynamics relationships in perovskite oxyhydrides and alkali silanides. Department of Chemistry and Chemical Engineering, Chalmers University of Technology; 2019.

[18] Lavén R. Dynamical properties of metal halide and oxyhydride perovskites Insights from inelastic neutron scattering. Department of Chemistry and Chemical Engineering, Chalmers University of Technology; 2019.

[19] Peña MA, Fierro JLG. Chemical structures and performance of perovskite oxides; 2001.

[20] Zhu J, Li H, Zhong L, Xiao P, Xu X, Yang X, et al. Perovskite oxides: Preparation, characterizations, and applications in heterogeneous catalysis. ACS Catalysis. 2014 9;4(9):2917-40.

[21] Yamamoto T, Zeng D, Kawakami T, Arcisauskaite V, Yata K, Patino MA, et al. The role of π-blocking hydride ligands in a pressure-induced insulator-to-metal phase transition in $SrVO_2H$. Nature Communications. 2017 12;8(1).

[22] Brice JF, Moreau A. Synthèse et conductivité anionique des hydruro-oxydes de lanthane de formule LaHO, $LaH_{1+2x}O_{1-x}$ et $LaH_{1+y}O_{1-x}$ (y < 2x). Ann Chim Fr. 1982;7:623-34.

[23] Ahmed I, Knee CS, Karlsson M, Eriksson SG, Henry PF, Matic A, et al. Location of deuteron sites in the proton conducting perovskite $BaZr_{0.5}In_{0.5}O_{3-y}$. Journal of Alloys and Compounds. 2008 2;450(1-2):103-10.

[24] Ahmed I, Eriksson SG, Ahlberg E, Knee CS, Berastegui P, Johansson LG, et al. Synthesis and structural characterization of perovskite type proton conducting $BaZr_{1-x}In_xO_{3-\delta}$ ($0.0 \leq x \leq 0.75$). Solid State Ionics. 2006 7;177(17-18):1395-403.

[25] Kanazawa T, Nishioka S, Yasuda S, Kato D, Yokoi T, Nozawa S, et al. Influence of the Hydride Content on the Local Structure of a Perovskite Oxyhydride $BaTiO_{3-x}H_x$. Journal of Physical Chemistry C. 2023 4;127(15):7546-51.

[26] Sakaguchi T, Kobayashi Y, Yajima T, Ohkura M, Tassel C, Takeiri F, et al. Oxyhydrides of (Ca,Sr,Ba)TiO_3 perovskite solid solutions. Inorganic Chemistry. 2012 11;51(21):11371-6.

[27] Schrader M, Mienert D, Oh TS, Yoo HI, Becker KD. An optical, EPR and electrical conductivity study of blue barium titanate, $BaTiO_{3-\delta}$. Solid State Sciences. 2008 6;10(6):768-75.

[28] Granhed EJ, Lindman A, Eklöf-Österberg C, Karlsson M, Parker SF, Wahnström G. Band: Vs. polaron: Vibrational motion and chemical expansion of

hydride ions as signatures for the electronic character in oxyhydride barium titanate. Journal of Materials Chemistry A. 2019;7(27):16211-21.

[29] Moore E, Smart L. Solid state chemistry : an introduction. Fifth edition ed. CRC Press; 2021.

[30] R1etveld HM. A Profile Refinement Method for Nuclear and Magnetic Structures; 1969.

[31] Von Dreele RB. THE RIETVELD REFINEMENT METHOD IN GSAS-II. Argonne National Laboratory;.

[32] Pecharsky VK, Zavalij PY. Fundamentals of Powder Diffraction and Structural Characterization of Materials Fundamentals of Powder Diffraction and Structural Characterization of Materials 1 2 3 Second Edition Second Edition;.

[33] Hallam KR, Darnbrough JE, Paraskevoulakos C, Heard PJ, Marrow TJ, Flewitt PEJ. Measurements by x-ray diffraction of the temperature dependence of lattice parameter and crystallite size for isostatically-pressed graphite. Carbon Trends. 2021 7;4:100071. Available from: https://www.sciencedirect.com/science/article/pii/S2667056921000481?utm_source=chatgpt.com.

[34] Patterson AL. The Scherrer Formula for I-Ray Particle Size Determination; 1939.

[35] Mccusker LB, Von Dreele RB, Cox DE, Louër D, Scardi P. Rietveld refinement guidelines. urn:issn:0021-8898. 1999 2;32(1):36-50. Available from: //journals.iucr.org/paper?gl0561.

[36] Coats AW, Redfern JP. Thermogravimetric Analysis A Review*;.

[37] Piovano A. Inelastic neutron scattering applied to materials for energy. In: EPJ Web of Conferences. vol. 104. EDP Sciences; 2015. .

[38] Ramirez-Cuesta AJ, Jones MO, David WIF. Neutron scattering and hydrogen storage. Materials Today. 2009 11;12(11):54-61.

[39] Kler J, De Souza RA. Hydration Entropy and Enthalpy of a Perovskite Oxide from Oxygen Tracer Diffusion Experiments. Journal of Physical Chemistry Letters. 2022;13(18):4133-8.

[40] PXRD: D8 Discover;. Available from: https://www.chalmers.se/en/infrastructure/cmal/instruments/x-ray-scattering/pxrd-d8-discover/.

[41] Toby BH, Von Dreele RB. GSAS-II: The genesis of a modern open-source all purpose crystallography software package. Journal of Applied Crystallography. 2013 4;46(2):544-9.

[42] DIFFRAC.EVA | Bruker;. Available from: https://www.bruker.com/en/products-and-solutions/diffractometers-and-x-ray-microscopes/x-ray-diffractometers/diffrac-suite-software/diffrac-eva.html.

[43] Thermal Analysis System TGA/DSC 3+ - Overview - METTLER TOLEDO;. Available from: https://www.mt.com/sg/en/home/products/Laboratory_Analytics_Browse/TA_Family_Browse/ta-instruments/thermal-analysis-system-TGA-DSC-3-plus.html.

[44] ISIS Tosca;. Available from: https://www.isis.stfc.ac.uk/pages/tosca.aspx.

[45] Pinna RS, Rudić S, Parker SF, Armstrong J, Zanetti M, Škoro G, et al. The neutron guide upgrade of the TOSCA spectrometer. Nuclear Instruments and

Methods in Physics Research, Section A: Accelerators, Spectrometers, Detectors and Associated Equipment. 2018 7;896:68-74.

[46] Al-Shakarchi EK, Mahmood NB. Three Techniques Used to Produce $BaTiO_3$; Fine Powder. Journal of Modern Physics. 2011;02(11):1420-8.

[47] Felgner KH, Müller T, Langhammer HT, Abicht HP. On the formation of $BaTiO_3$ from $BaCO_3$ and TiO_2 by microwave and conventional heating. Materials Letters. 2004 5;58(12-13):1943-7.

[48] Gunter JR, Marks Olaf, Hofer F. Electron microscopy of barium ortho-titanate and the products of its reaction with carbon dioxide. Reactivity of Solids. 1988;6:217-30.

[49] Vedmid' L, Fedorova O, Uporov S, Sterkhov E. Structural and Magnetic Characteristics of Gadolinium Manganite Modified with Barium $Gd_{0.9}Ba_{0.1}MnO_3$. Journal of Superconductivity and Novel Magnetism. 2022 5;35(5):1141-50.

[50] Shannon Radii;. Available from: `http://abulafia.mt.ic.ac.uk/shannon/ptable.php`.

A

Appendix 1

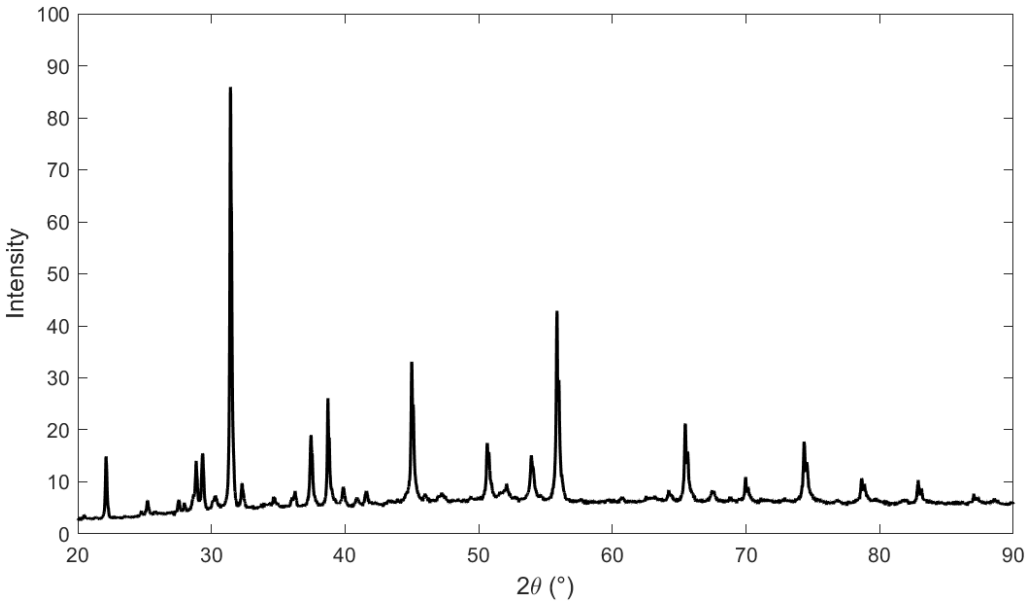

Figure A.1: PXRD pattern of CaH_2 reduced synthesised $BaTiO_3$ in an alumina tube at 600^{o}C for 48 hours. Plotted in Matlab.

DEPARTMENT OF CHEMISTRY AND CHEMICAL ENGINEERING
CHALMERS UNIVERSITY OF TECHNOLOGY
Gothenburg, Sweden
www.chalmers.se

CHALMERS
UNIVERSITY OF TECHNOLOGY